UNIVERSITÀ DEGLI STUDI DI PADOVA

DIPARTIMENTO DI SCIENZE CHIMICHE

CORSO DI LUREA MAGISTRALE IN CHIMICA

TESI DI LAUREA MAGISTRALE

Synthesis of Co-doped anisotropic $YbFeO_3$ microparticles and their exsolution behaviour

Relatore: Prof. ssa Silvia Gross

Correlatore: Prof. Simone Mascotto

Controrelatore: Prof. Christian Durante

LAUREANDA: Beatrice Tonin

ANNO ACCADEMICO 2022/2023

Table of Contents

1 List of acronyms

BE	Backscattered Electrons
DESY	Deutsches Elektronen-Synchrotron
EDX	Energy Dispersive X-Ray
EXAFS	Extended X-Ray Absorption Fine Structure
LPG	Liquefied Petroleum Gas
MS	Mass Spectrometry
OER	Oxygen Evolution Reaction
PE	Primary Electrons
PXRD	Powder X-Ray Diffraction
SE	Secondary Electrons
SEM	Scanning Electron Microscopy
TPR-H_2	Temperature Programmed Reduction
XANES	X-Ray Absorption Near Edge Spectroscopy
XAS	X-Ray Absorption Spectroscopy

2 Structure of the Thesis

This thesis is structured in 8 Chapters. Chapters 1 and 2 present the List of the Acronyms and the Structure of the thesis, respectively. Chapter 3 provides an introduction to the thesis and presents the research objectives. Chapter 4 presents the main topics on which this work is based, including the corresponding state of the art. The importance of nanomaterials in modern science is discussed. The main characteristics of perovskites are then described, with a focus on ferrites. Thereafter, the hydrothermal synthesis is illustrated and the associated mechanism for the synthesis of ytterbium ferrite according to the literature is presented, followed by a brief presentation of anisotropic particles as a new frontier in materials development. Finally, the exsolution process and its advantages in the preparation of catalysts is described. The experimental procedures are described in detail in Chapter 5, while characterisation methods are given in Chapter 6. In Chapter 7, the results obtained from the characterisation of the materials synthesised and processed using the exsolution method are presented and discussed. In Chapter 8, the most significant results obtained from the research are summarised and future prospects are outlined.

3 Introduction

Catalysis is fundamental to change the global energy scenario and the quality of human life: with electrocatalysis and photocatalysis it will be possible to convert water to hydrogen/oxygen and CO_2 to solar fuels. The continuous evolution and optimization of catalysis systems is fundamental, and it is driven by rational catalyst design, novel discovery methods, and the demand for suitable, cost-effective processes. The fields in which catalysis is most involved are pharmaceutical, energy conversion, production of fine chemicals and other sectors, including food, petrochemicals and oil refining [1,2]. The characteristics that are required for new generation catalysts are high activity, stability, selectivity and the replacement of noble metals (Pt, Rh, Ir) with more abundant and sustainable metals. An excellent class of materials with encouraging characteristics to meet these requirements are perovskite oxides, identified by the formula ABO_3. The flexibility of the structure of perovskite, which can accommodate around 90% of the natural metallic elements of the periodic table, leads to an immense range of possible physico-chemical properties that allow materials to be customised for specific applications [3–5]. Nevertheless, the exceptional stability and abundance of forming elements make perovskite oxides promising materials for the improvement of environmental catalysis [4]. Recently, rare earth orthoferrites ($REFeO_3$) have attracted particular attention due to their remarkable thermal and chemical stability, and special electrical, catalytic and magnetic properties [6,7]. This catalytic activity can be even further enhanced by means of the exsolution method, which represents a sustainable approach for the preparation of metal-ceramic composite materials with tuned and well-distributed metal nanoparticles. Exsolution leads to the decoration of material's surface by the migrations of B-site metal dopants upon their reduction in the perovskite matrix. The nanoparticles obtained by exsolution are "anchored" to the perovskite's support, hence they possess exceptional stability and resistance to sintering and poisoning. The use of a perovskite matrix is advantageous because it allows catalysts to be designed in terms of the chemical nature, dispersion and adaptability of the dissolved nanoparticles simply by varying the composition of the perovskite. Moreover, the

catalysts prepared via exsolution exhibit enhanced catalytic activity and improved lifetime owing to the reversibility of the process in oxidative conditions [8].

The optimisation of the chemical reactivity of surfaces and interfaces is another important area of current research, as unique physical and chemical processes can take place there. Anisotropic microparticles have attracted considerable research interest in light of their unique attributes. Taking advantage of their anisotropic nature, these microstructures allow different functions and properties to be combined in a single entity [9]. Consequently, the catalytic properties of the nanoparticles are also influenced by the orientation of the surface and structure of the host metal oxide [10]. Furthermore, it has been outlined that, by precisely adjusting the orientation of the crystal planes, it is possible to influence the properties of the material. These include, for example, reactivity, catalytic activity, strength and optoelectronic properties related to the separation of charge separation.

Another key and challenging research in contemporary chemistry and materials science is the precise architectural manipulation of nanocrystals with well-defined morphologies and accurately tunable dimensions. The growing demand for the development of new environmentally friendly techniques for the preparation of nanostructures has become one of the new frontiers of modern research. One of the methods that has proven to be an efficient and economical process for the preparation of various inorganic materials with different controllable morphologies and architectures is the hydrothermal synthesis [11–13]. Hydrothermal synthesis is an heterogenous chemical reaction that takes place in aqueous media, above room temperature (normally above 100 °C) and at a pressure greater than 1 atm within a sealed vessel [13]. The exsolution of catalytically active nanoparticles on particles with different morphologies is a promising and captivating topic in nanomaterial science. First of all, the combination of exsolution and facet dependency has not yet been thoroughly investigated and understood. In addition, various crystal facets are characterised by different surface energies and stability. This has an impact on the nucleation dynamics of the exsolution phenomenon leading to “preferential nucleation sites” [14]. This makes it possible to specifically modify the chemistry and energy of particular facets and prepare nanomaterials with unique and unconventional properties.

3.1 Aims of the Thesis

The aim of this thesis work was to hydrothermally synthesise anisotropic particles of ytterbioferrite ($YbFeO_3$) doped with cobalt. The three different morphologies obtained were: cuboids, elongated tetragons and bipyramids. The pure microparticles were treated at different temperatures, in the range of 500 to 900 °C, under reducing atmosphere of H_2 to investigate the behaviour of the material. The Co-doped microparticles were then treated in a reducing atmosphere at 500°C and 550°C to perform metal exsolution. Of particular interest was the study of the behaviour of the synthesised material under these conditions and the investigation of a possible preferential exsolution of nanoparticles on the different faces characterising the different morphologies.

4 Theoretical Background

4.1 Nanomaterials in contemporary science

Heterogeneous catalysis plays a crucial role in the chemical and energy industries and is essential to achieve carbon-neutral operations [15]. The primary goal is to design highly active and durable catalytic processes that can have a positive impact on the world. The pursuit of rational design in catalysis has become increasingly urgent in recent years due to the growing demand for energy, the need for sustainable processes and rising CO_2 emissions. Catalytic processes are crucial for the production of chemicals and represent a significant part of industrial energy use; improving their efficiency offers significant opportunities to reduce energy consumption and environmental impact. This is particularly important for processes such as CO_2 reduction [16], hydrogen production [17], methane oxidation [18] and ammonia production [19,20]. In the context of heterogeneous catalysis, where the reactions primarily occur at the interface between the reaction mixture and the catalyst, increasing the surface area to extend the reaction boundaries is fundamental to augment the catalytic activity. Thus, reducing the size of the metal particles, ideally to the nanoscale, maximises the surface-to-volume ratio as well as ensures superior surface dispersion of nanoparticles through the substrate, draw the economic utility out of the final catalyst.

The field of Nanoscience and Nanotechnology has obtained special importance and is revolutionising science and technology, addressing various industrial, electronic, security, drug delivery and environmental challenges [21]. Nanomaterials, in particular nanoparticles between 1 and 100 nm in size, have broad applications in medicine, cosmetics, packaging and electronics due to their unique magnetic, catalytic, mechanical, optical and electronic properties. The properties of nanoscale materials are highly dependent on surface atoms and can be controlled through methods such as concentration limitation and surface functionalisation [22].

Nanomaterials exhibit high activity in various applications, such as hydrocarbon catalysis, electrochemical conversion, and photochemistry. Especially, metal

nanoparticles are the key functional component in various nanotechnological applications [23]. Supported nanoparticle systems have received increasing attention in recent decades due to their potential to achieve high activity levels [24]. Traditional methods like impregnation, co-precipitation, or deposition have been employed to disperse nanoparticles across a support. However, these methods often result in limited control over size distributions and weak interaction between the support and metal nanoparticles, leading to disappointing low longevity of the catalytic system. Short catalyst's lifespan is a common concern and is particularly critical in clean energy conversion technologies. Nevertheless, their nanoscale nature requires very precise designs and construction methods. Recently, a novel material design approach, known as "ex-solution", has emerged. This approach offers a straightforward, single-step and highly controllable pathway to create supported nanoparticles spontaneously generated directly from the support. The catalysts obtained through this process are characterised by high stability against agglomeration and poisoning, and high activity across a range of applications [25,26].

Perovskite-structured oxides represent one of the most promising class of materials in the field of heterogenous catalysis due to their acceptable catalytic activities and robust thermal stability. However, the utilisation of perovskite oxides is restricted when compared to noble metal catalysts because the most stable surface is usually terminated with non-catalytically active crystal facets [27]. To address this issue, a recent breakthrough in the realm of technology and specialised catalyst design involves the innovative combination of anisotropic microparticles and exsolution. This approach holds great promise for advancing the field and optimizing catalyst performance.

4.2 Perovskite structure and properties: a special class of materials

Historically, perovskite, was named after the Russian mineralogist L. A. Perovski (1792-1856), identifies a calcium titanate oxide mineral with the chemical formula $CaTiO_3$. Characterized by a yellow, brown, or black colour it was first discovered by Gustav Rose in 1839 [28]. Nowadays the term perovskite oxides refers to a vast class of compounds characterised by the same type of crystal structure as $CaTiO_3$ [29]. This family of minerals exists extensively in nature [30], such that some scientists believe $MgSiO_3$ to be the most abundant mineral in the mantle of the earth [31]. The basic structure of perovskite oxides is ABO_3. It consists of a tightly packed arrangement of oxygen anions (or halides, in the case of ABX_3 perovskites) [32], with two types of sites for the cations. "A" can be a lanthanide, alkaline, or alkaline-earth cation and "B" usually, is a transition metal cation such as Co, Fe, Cr, Ni, Mn and Ti. The ideal unit cell of perovskite oxides is cubic from the space group Pm3m, in which the smaller B-site cations are surrounded by an octahedron of X-site anions in a 6-fold coordination, while the larger A-site cations occupy the interstitials formed by corner-sharing BX_6 octahedral and have coordination number of 12 [33]. The material has high structural stability, and the A and B sites can be replaced by any metal or semi-metal from the periodic table [34] leading to a variety of perovskite oxide solid solutions with general formula $A_{1-x}A'_xB_{1-y}B'_yO_{3\pm\delta}$. Where "+" denotes oxygen excess and "−" an oxygen deficiency as a consequence of non-stoichiometry introduced with the substitution [35]. A distortion in the crystalline structure with respect to the ideal cubic unit cell, and possibly the collapse of the perovskite structure, may result from the inclusion of multiple A or B cations with different sizes and valences. These deviations are quantified with the Goldschmidt tolerance factor (t) [36]:

$$t = \frac{r_A + r_O}{\sqrt{2}\,(r_B + r_O)}$$

with r_A , r_B and r_O being the ionic radii for the A-site cation, B-site cation and oxygen respectively. Ideally, t should be equal to 1.0, and it has been found empirically that when 0.9 < t < 1.0, the cubic perovskite structure is stable. When 0.71 < t < 0.9 orthorhombic or rhombohedral unit cells are observed. This occurs when the A-site cation size is too small, which leads to a lowering in the symmetry of the unit cell. If the A-site cation is too large compared to the B-site cation, the tolerance factor becomes larger than the unity. Under these conditions, hexagonal or tetragonal symmetries are the most stable. As a consequence of this tilt and rotation of the B-site octahedra there is a change in the B—O bond angles and thus the hybridization of the electronic orbitals is affected [37]. In addition, some perovskites (e.g. $BaTiO_3$ and $KNbO_3$) show distortions when cooled below their Curie temperature. If one of the cations is significantly larger than that required for the ideal cubic structure, the displacement of the smallest cation can form dipoles, which align within the material when an electric field is applied. This property allows high polarisability and permittivity and leads to ferroelectricity [6].

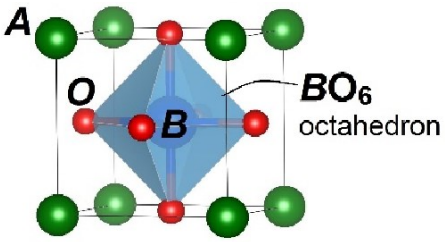

Figure 1. Ideal cubic (space group Pm3m) perovskite crystal structure [38].

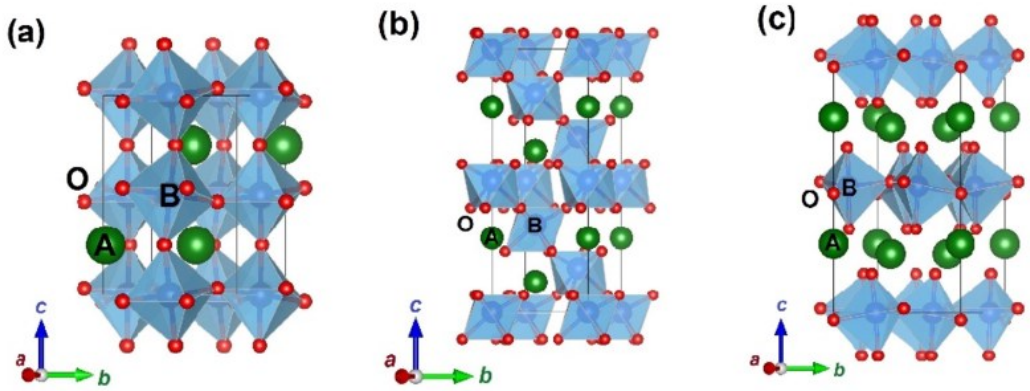

Figure 2. The distorted ABO_3 perovskite crystal structures with (a) orthorhombic (space group: Pbnm), (b) rhombohedral (space group R3c), and (c) hexagonal (space group: P63cm) symmetry [38].

The flexibility of the perovskite structure offers a way to tailor the electronic properties of the material as well as B—X bond length and strength. The replacement of the A and B sites with cations of a different nature can lead not only to distortions of the crystal lattice, but also to the insertion of extra charges that are counterbalanced by the formation of structural defects (oxygen or cationic vacancies). This has fundamental consequences on the functional properties of the material since diffusion of species (charged and neutral) through crystalline solids depends on the defect structure. Therefore, a great variety of perovskite oxides can be synthetised and engineered, with different surfaces and morphologies (e.g. bulk, nanosized and porous) depending on the intended use [39].

When the positions of the B-site cation are mainly occupied by Fe^{3+} and the symmetry of the unit cell is orthorhombic, the perovskites are identified with the name of ortho-ferrites[7]. Ortho-ferrites are semiconductor materials with magneto-optical, ferroelectric and ferromagnetic properties [40–42]. The distorted structure of perovskite, in which the magnetic moment of the Fe^{3+} cation is tilted, makes orthoferrites weakly ferromagnetic [42]. The magnitude of magnetism is influenced by Fe-O and R-O interactions, which is why the choice of R is assumed to be critical [41]. Ferroelectricity results mainly from Fe-Fe, Fe-R and R-R interactions [42].

Since the beginning of this millennium, rare-earth ortho-ferrites ($REFeO_3$) have attracted particular interest due to their special electrical, catalytic and magnetic properties [43,44], which make them interesting materials in various research fields such as catalysis [45], ferromagnetic and ferroelectric storage [46] and gas sensors [42].

Rare-earth ortho-ferrites are also distinguished by their non-toxicity and chemical stability which, in combination with their electrical properties, make them attractive alternatives to conventional absorbers in solar cells [47].

$YbFeO_3$ in bulk form occurs in the crystal structure of thermodynamically stable orthorhombic perovskite. Furthermore, two metastable hexagonal phases are present in the nanostructured thin films, which are of interest for other applications, especially in photocatalysis [48]. The cation Yb^{3+} occupies the A sites of the perovskite structure. Being relatively small (ionic radius r = 1.042 Å), due to the f orbitals, the crystal cell structure of $YbFeO_3$ is distorted with respect to the cubic system. The reference values of the individual lattice parameters vary in the literature to the second or third decimal

place. Zhang et al. [49] (work on which part of the synthesis used in this thesis is based) report the following lattice parameters: a = 5.2355 Å, b = 5.5686 Å and c = 7.5843 Å. Rare-earth orthoferrites are semiconductors[50]. The band gap of $YbFeO_3$ nanocomposite (47 nm) orthorhombic is 2.15 eV [51].

4.3 Hydrothermal Synthesis

Historically the word *hydrothermal* was firstly used by the British geologist, Sir Roderick Murchison (1792 – 1871), to describe the formation process of various rocks and minerals in the earth's crust carried out by the action of water at an elevated temperature and pressure. This natural phenomenon that leads to the formation of many of the minerals found in nature (said to be "of hydrothermal origin") has aroused scientific interest since the beginning of the 19th century, when the first experiments began to attempt to reproduce such reaction conditions in the laboratory. Its development was soon a success, and the hydrothermal method is now widely employed in the large-scale production of piezoelectric, magnetic, optic, ceramic and many other materials, both as single crystals and polycrystalline [52].

In chemistry a *hydrothermal reaction* is defined as *"any heterogeneous chemical reaction in the presence of a solvent (aqueous or solvothermal) above room temperature and at pressure above 1 atm in a closed system"*, according to the Handbook of Hydrothermal Technology [53]. This synthesis is carried out in a closed system in which a high pressure is reached as a result of heating. Under such conditions, the properties of the solvent (ionic product, viscosity, ionic constant and solvating power) change significantly [54,55], allowing the reagents, which are otherwise difficult to dissolve, to go in solution and subsequently form crystalline structures at relatively low temperatures [56]. These synthesis conditions can be achieved using either a common autoclave, which subjects the system to externally generated heat and pressure, or a bomb autoclave [57]. In this closed vessel, pressure is generated autogenously as a response to external heating and is directly proportional to temperature. Inside the reaction container a solvent-vapour system persists at higher temperatures than the normal boiling point [58]. The volume of the reaction mixture that fills the vessel also

plays a crucial role in defining the conditions that will be created within the system. Usually, in case of water as solvent with a filling ratio above 32%, as the temperature increases, the vapour-liquid interface will gradually rise, expanding the liquid phase until it fills completely the entire system. Hydrothermal (or more generally solvothermal) synthesis can be carried out in both supercritical, if temperature and pressure in the system are greater than their critical values, or subcritical conditions. A quite recent use of the hydrothermal method is that for the synthesis of mixed oxides in nanocrystalline form [59,60]. The hydrothermal method of crystal growth has several advantages over the conventional wet-chemistry techniques. First, the ability to conduct reactions at low temperatures is advantageous. Additionally, the closed system enables the investigation of the influence of temperature, pressure and compositional variations individually. This enables a good control over particle size by adjusting the temperature treatment and the composition of the reaction medium. The steps of crystal formation from a solution are the dissolution of the precursors in the liquid phase with the generation of a supersaturated mixture, from which the ordered solid structures can slowly precipitate. Fundamental in this process are the crystal seed formation (nucleation) and the ordered crystal growth around them. Different syntheses are characterised by different kinetics of these two steps; accordingly, the resulting material are different. A single large crystal will result when the precipitation is slow, while a large number of small crystals will be obtained if the formation of the nucleation seeds prevails over their growth.

In this thesis work, the hydrothermal synthesis under subcritical conditions was exploited to prepare a crystalline powder of undoped and Co-doped $YbFeO_3$. The formation mechanism of $YbFeO_3$ crystallites can be described with the following reactions:

$$Yb^{3+} + 3OH^- \rightleftarrows Yb(OH)_{3(s)} \;\; ; \;\; Fe^{3+} + 3OH^- \rightleftarrows Fe(OH)_{3(s)}$$

$$Yb(OH)_{3(s)} + OH^- \rightleftarrows Yb(OH)_4^- \;\; ; \;\; Fe(OH)_{3(s)} + OH^- \rightleftarrows Fe(OH)_4^-$$

$$Yb(OH)_4^- + Fe(OH)_4^- \rightarrow YbFeO_{3(s)} \downarrow + H_2O$$

Alkalinity plays a crucial role in controlling these processes. The addition of KOH leads to the transformation of Yb and Fe ions into amorphous hydroxides, followed by dissolution and the formation of hydroxyl complexes such as $Yb(OH)_4^-$ and $Fe(OH)_4^-$ by the action of the mineraliser. These complexes might act as crystal growth units and eventually dehydrate to form crystalline cores, leading to the precipitation of insoluble $YbFeO_3$ particles from a supersaturated hydrothermal solution [41].

4.4 Anisotropic Microparticles

Anisotropic microparticles have gained significant scientific interest due to their unique properties, complex components, and versatility in various applications [61]. The combination of various functions within a single particle due to the complex morphologies and diverse components, unlocks a broad range of possibilities in practical applications such as displays, sensing, drug delivery and cell culture [62,63]. Introducing anisotropy into any particles for various shapes, sizes and monodisperse morphologies, generates different facets with different surface energies. This leads to novel physical and chemical properties and allows for tailored applications in areas such as catalysis, optoelectronics, and more [9].

Anisotropic nanomaterials are classified as 1D, 2D, and 3D structures and exhibit directional-dependent properties as a result of the motion of electrons in different dimensions, influencing properties like reactivity, catalytic activity, resistance, and optoelectronics characteristics. Particle shapes are closely linked to crystallographic surfaces that enclose the particles, further influencing their properties and potential applications [64]. The variation in the number of atoms on the surface of different facets, leads to distinct reactivities, with edges and corners often showing enhanced reactivity compared to other sites. Controlling the crystal shape and facet of crystals micro- and nano-structures has become essential in material design [65].

The synthesis of complex nano-catalysts, in particular bimetallic nanoparticles, has opened up new possibilities by altering atomic and electronic arrangements. The combination of rare elements such as Au, Pt and Pd with more abundant metals like Ni, Cu, Co and Fe has improved catalytic activity, selectivity and stability [40]. Perovskite

oxides, known for their high thermal stability, could benefit from high-index facet tailoring to enhance their activity [40].

There are numerous chemical and physical methods for producing microparticles and they are categorised as either “top-down” or “bottom-up” approaches, with the second family being considered to be more straightforward and precise for the production of small particles [66]. However, the synthesis of high-quality single crystals with well-defined shapes and facet control is still a challenge. Solvothermal synthesis is one of the possible approaches for the synthesis of anisotropic particles from controlled crystallisation of molecular or atomic building blocks from solution. This method allows to obtain a wide range of particles in terms of shape, size and composition from the nanometre to the micrometre scales [67]. Many studies have been performed to obtain anisotropic perovskite-based particles by solvothermal synthesis [68–71]. Extensive research has focused on the solvothermal synthesis of the perovskite material $BeFeO_3$, resulting in various crystal structures through the manipulation of synthesis parameters. These structures exhibit a wide range of properties, extending their use from photocatalysis to dielectric applications [11,72]. In the field of the solution synthesis of rare-earth ferrites ($REFeO_3$ where RE = lanthanide or Y), Yuan et al. successfully obtained, via hydrothermal method, tailored crystal shapes by just adjusting the KOH to urea molar ratio [40]. They found that the ratio of mineraliser to urea concentration plays an important role in the outcome of the synthesis. In particular, it is the urea (or NH_4^+) that plays a key role in the control of the preferential exposed facets of the crystals. As a matter of fact, without the addition of urea or NH_4^+ species, no anisotropy would be pursued. The proposed function of the urea is to release NH_4^+ upon decomposition. The ion, due to its small size, positive charge and tetrahedral symmetrical structure interacts with the BO_6 octahedral groups of the perovskite structure, via hydrogen bond. This coordination can take place through an eclipsed conformation or a staggered conformation (Figure 3). In the case of perovskites oxides with distorted BO_6 octahedron, due to the different sizes between the A-site and the B-site cations, the staggered conformation is the most stable. In this way the NH_4^+ ions act as a capping agent blocking the growth of crystals along specific crystallographic directions.

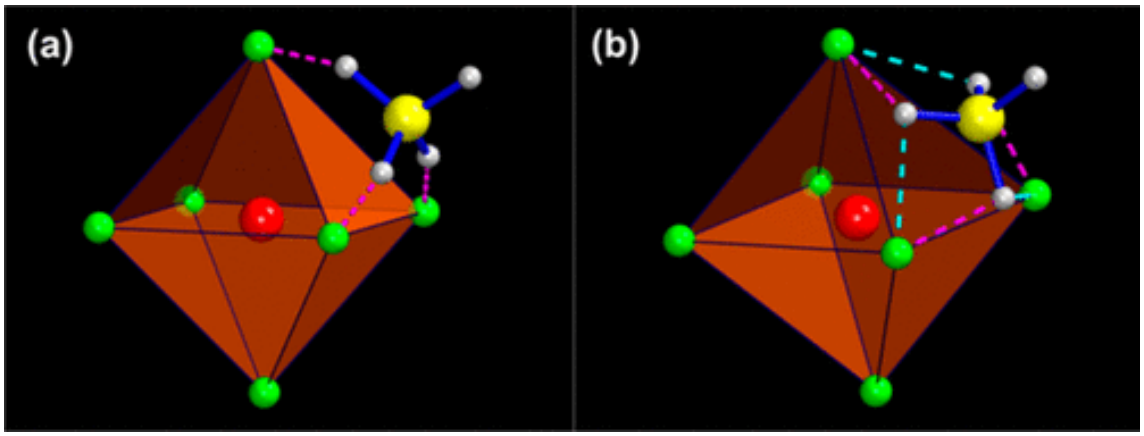

Figure 3. Possible coordination ways of NH4+ to BO6 octahedron: a) eclipsed conformation and b) staggered conformation. B-site cation in red; O in green; N in yellow; H in grey [40].

Another study of fundamental importance for this thesis work is the one reported by Zhang and co-workers concerning the hydrothermal synthesis of anisotropic $YbFeO_3$ microparticles with different morphology depending on the base used (KOH or NaOH) and the urea concentration [49]. In this work, the influence of the type of the mineraliser as well the urea concentration effect on facet growth of $YbFeO_3$ was explored under mild hydrothermal conditions (200 – 260 °C for 72 hours). They report how the nature of the base as well as the amount of the urea has a crucial impact on the shape evolution of the crystal. Mineralisers generate different ions in solution (K^+, Na^+ and NH_4^+), which act as stabilisers of the different facets and thus promote the growth of some facets over others. In Figure 4 the six crystal facets groups that were found to mainly compose the $YbFeO_3$ microparticles are shown. The {110}, {101} and {220} are charged balanced while the {020}, {111} and {021} present strong negative charges due to the exposure of FeO_6 octahedrons.

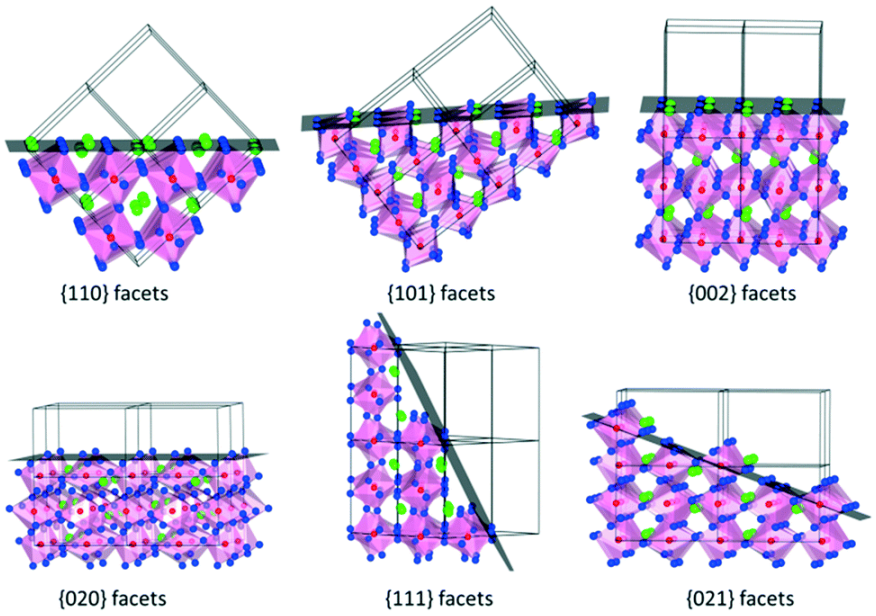

Figure 4. Structures of different crystal facets of $YbFeO_3$ perovskites. Fe in red; Yb in green, O in blue [49].

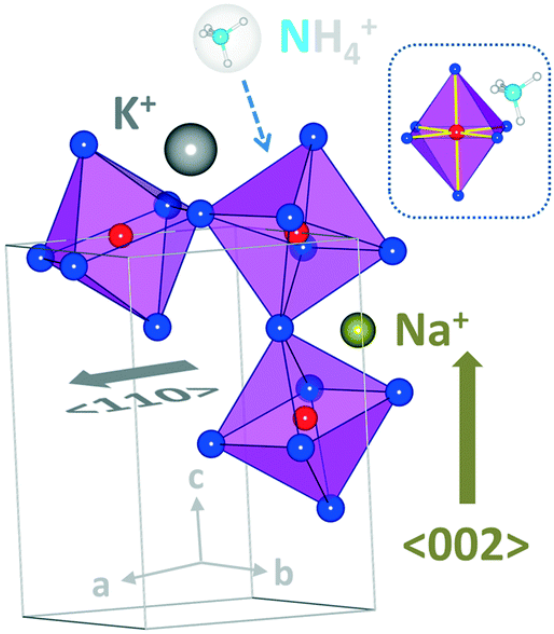

Figure 5. Effect of NH_4^+, K^+ and Na^+ ions on the crystal growth of $YbFeO_3$ [49].

Figure 5 represents the stabilisation effect of mineraliser cations during the hydrothermal synthesis. The orthogonal $YbFeO_3$ presents two different types of tilting between the FeO_6 octahedra distinguished by the width of the open space. The large K^+ (1.38 Å) can easily accommodate in the bigger gap, while Na^+ (1.02 Å) and NH_4^+ in the smaller ones [73]. From this derives the different facets stabilisation and their consequent growth speed. Moreover, as discussed above, the non-spherical symmetric

cations of NH_4^+ bound to the FeO_6 via hydrogen bonding not only stabilising the surface charge of the faces, but also retarding the growth along the corresponding crystal directions. The concentration of ions in the reaction mixture and their ratios, has a fundamental role in determining the final shape of $YbFeO_3$ microparticles.

The hydrothermal synthesis of Co-doped $YbFeO_3$ reported in this work is mainly based on the study of Zhang et al. [49] and on previous research carried out in Mascotto's group where the hydrothermal synthesis of anisotropic $YbFeO_3$ was explored and promising results were obtained using KOH as mineraliser and different KOH to urea molar ratios.

4.5 Exsolution

Exsolution is a remarkable phenomenon that has gained increasing attention in recent years especially in the field of material science and catalysis. This process involves the selective emergence of metallic nanoparticles from catalytically active cations dissolved within an oxide support upon partial reduction. Exsolution follows the classical nucleation theory [26]. The key steps of the process include the formation of a solid solution phase, exposure to reducing conditions, and the diffusion of ions, oxide ions and electrons across the host oxide lattice to initiate nucleation and growth of metallic nanoparticles. Essentially, exsolution is a phase decomposition process influenced by surface and bulk defects end external conditions. Nucleation primarily occurs at the surface, but can also happen within the bulk of easily reducible host lattices. Exsolution can occur on various support morphologies, including dense, porous, loose powder and thin film. The driving force for the process can be provided by reducing gasses, electrochemical forces, or light, with high-temperature reduction being the most common method [26].

The perovskite (ABO_3) lattice is the preferred choice for the exsolution due to its versatile properties, as it can accommodate various cations of different sizes, coordination numbers and charges [25]. The characteristics of the exsolution depend on a very large number of variables and can be controlled by intrinsic (composition and structure) and extrinsic (temperature, atmosphere, etc.) parameters. The type of metal

involved plays a critical role in determining whether exsolution is thermodynamically favourable. Alkaline earth metals (e.g., Ca, Sr, Ba, and La) typically have ΔG of reduction values greater than zero, making exsolution less likely, while most 3d transition metals (e.g., Fe, Co, and Ni) have negative ΔG values at elevated temperatures, making them more prone to exsolution [26]. Additionally, A-site deficiency in perovskites ($A_{1-\alpha}BO_3$) has been found to enhance B-site exsolution. This deficiency acts as a driving force to bring the perovskite structure back towards a stable ABO_3 stoichiometry during metal exsolution at site B. The exsolution process involves the introduction of oxygen vacancies (δ) during the reduction of an A-site deficient perovskite. These vacancies destabilise the perovskite lattice, leading to the spontaneous exsolution of the B-site metal to maintain stoichiometry [33]. This reaction can be expressed as:

$$A_{1-\alpha}\,BO_{3-\delta} \rightarrow (1-\alpha)ABO_{3-\delta'} + \alpha B$$

Exsolution can be controlled by manipulating the amount of oxygen vacancies (δ), which is related to the number of reduced B-site metal ions (BB'). This relationship is usually expressed with the Kröger-Vink notation for defects [74]:

$$2B_B^X + O_O^X \rightarrow 2B_B' + V_O^{\cdot\cdot} + \frac{1}{2}O_2$$

In addition, the exsolution process involves several energy-related aspects, such as activation energy, surface energy, strain energy, segregation energy, redox reaction energy, and crystal lattice energy, which are crucial for understanding its dynamics and thus for tailoring its outcome [25].

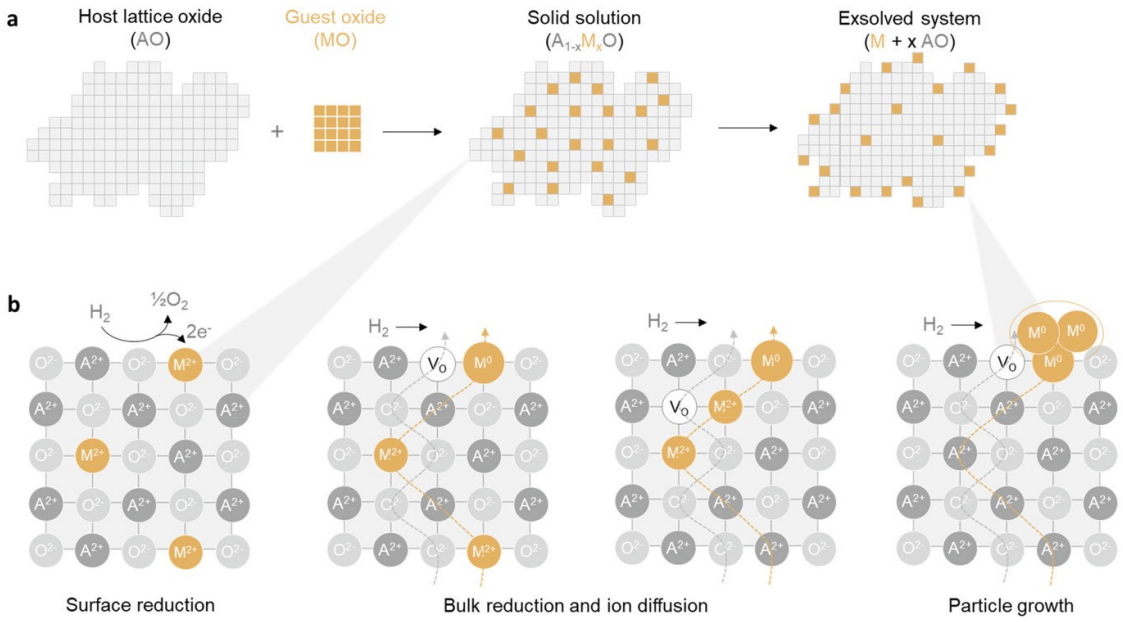

Figure 6. Schematic illustration of the process a) The exsolution method and b) key processes fundamental to exsolution [25].

The exsolution approach has revealed several advantages compared to deposition processes in the preparation of supported nanoparticles. One key advantage is the alignment between the host phase and the exsolved nanoparticles, which results in "socketed" in the support [75]. This offers unique properties. First, the nanoparticles are resistant to sintering and can redissolve into the oxide lattice under oxidative conditions, enabling material regeneration, preventing agglomeration and extending the material's lifespan [76]. Second, the partial embedment within the oxide matrix protects them from poisoning. Moreover, the exsolved particles are found to be more active than deposited counterparts, due to their particular strain they are subject to [25]. This makes exsolution an efficient, precise and straightforward process to obtain highly versatile and tailorable materials that find application in various fields, including catalysis, energy conversion and storage, oxygen transport and exchange and strain engineering.

The most commonly exsolved elements are Ni, Co, and Fe widely used in applications such as electrochemical conversion and hydrocarbon catalysis. It is worth mentioning that some great attention has been paid to exsolution of Fe-based perovskites, but it resulted to be very challenging to exsolve single metal nanoparticles from Fe-based perovskites. Certain metals, such as Fe, might not undergo exsolution if they are the only species occupying the perovskite's B-sites due to their high segregation energy.

Exsolution could become possible if they are accompanied by a second metal (often Ni or Co) with a lower segregation energy. This is because, in mixed cation systems, the presence of both metals increases the total energy of the perovskite system. Thus, the Co-Fe bonds, for example, would have lower formation energy than the Fe-Fe bonds [77]. These bimetallic systems have raised particular attention since they present particular stability and enhanced catalytic activities. Moreover, the exsolution of alloy nanoparticles allows to obtain synergic systems with the properties of different metals [78]. In particular Fe-Co exsolved nanoparticles have found applications in various solid oxide fuel cells (SOFC) for the oxidation of different kinds of fuels (e.g. H_2, LPG, C_2H_5OH and CH_3OH) [79], OER[77], and they have been successfully used also in electrolysis of H_2O and CO_2 and chemical looping reactions showing high catalytic activity, stability and conductivity [80].

Various interesting studies demonstrate that the perovskite oxide crystal orientation affects exsolution [81]. Neagu et al. conducted a comparative study on the exsolution behaviour of various terminations or plan orientations of $La_{0.4}Sr_{0.4}Ni_{0.03}Ti_{0.97}O_{3-\delta}$. Orientation (110) is rougher and thus shows priority exsolution over (100) and (111). This can be attributed to a reduction in the nucleation barrier resulting from the presence of crystal defects [75]. Kim et al. investigated $La_{0.2}Sr_{0.7}Ti_{0.9}Ni_{0.1}O_{3-\delta}$ thin films with three different crystal orientations [14], and the surface energy of $LaCaNiTiO_3$ (LCNT) on various crystal facets finding that the exsolution of Ni particles is preferential on the facets with lower interfacial energy [82]. These fascinating observations suggest that surface orientation and configuration play a key role in modifying the nucleation energy barrier, thereby influencing particle size distribution and surface coverage. Specifically, the dependence of the energy of segregation (E_{seg}) on specific orientations and terminations appears to correlate with the metal-to-oxygen atomic ratio on the surface [83]. This confirm that the design and preparation of perovskite catalysts with specific crystalline facets are crucial for enhancing catalytic activity through controlled exsolution and uniform distribution of active metals [8,84].

5 Experimental Procedures

5.1 Chemicals

In Table 1 the chemicals employed for the synthesis are listed.

Chemical	Molar Mass [g/mol]	% Purity	CAS number	Supplier
$Yb(NO_3)_3 \cdot 5H_2O$	359.07	99.9	35725-34-9	Abcr
$Fe(NO_3)_3 \cdot 9H_2O$	403.99	98+	7782-61-8	Alfa Aesar
$Co(NO_3)_3 \cdot 6H_2O$	291.04	98	10026-22-9	Fisher Scientific
KOH	56.11	99.98	1310-58-3	Abcr
CH_4N_2O	60.06	≥ 99.5	57-13-6	Sigma-Aldrich

Table 1. List of all the chemicals used for the synthesis.

5.2 Hydrothermal Synthesis of $YbFeO_3$

Initially, the hydrothermal synthesis of anisotropic microparticles of ytterbium ferrite was performed, based on the synthesis of Zhang et al. [49] and a previous study carried out in our laboratory in which the synthesis of this material was optimised by exploring various reaction conditions.

The following synthesis protocol was used. 2.5 mL of a clear, yellow solution of $Fe(NO_3)_3$ and 2.5 mL of a clear colourless solution of $Yb(NO_3)_3$, each at a concentration of 0.4 M, were prepared and mixed under stirring with a magnetic stirrer in an Erlenmeyer flask. Also under stirring, potassium hydroxide (KOH) was added, and heat developed in the mixture as a consequence of this addition. Once the orange-red viscous mixture had cooled to room temperature, urea was added in such quantities as to obtain the appropriate mineraliser to urea molar ratio (see Table 2). The reaction mixture was left under stirring until it turned completely homogeneous. The mixture was then transferred into a 10 mL Teflon liner, which was filled to 80% of the total volume. The Teflon liners were placed in a stainless steel reactor in an oven (200 – 230 °C) for 72 hours. Different temperatures from 200 to 230 °C with variations of 10 °C were explored to test their effect on the purity and morphology of the microparticles.

When the reaction was complete, the aqueous phases with a pungent ammonia odour were separated from the reddish solid phase of the product. The solid phase was first placed in a pulsed ultrasonic bath with deionised water for 30 minutes (37 kHz, 100% power at room temperature) for initial cleaning. The next two washing steps of the product were performed using a vortex. For each washing step, the solid phase was separated from the aqueous phase by centrifugation for 10 minutes (10,000 rpm). The resulting powder was dried overnight in a desiccator at 70 °C and then transferred into a glass vial. The product was characterised by X-ray powder diffractometry (P-XRD) and scanning electron microscopy.

The microparticle morphology depends on the KOH to urea molar ratio in the reaction mixture. The temperature also affects the shape of the microparticles. In Table 2 the molar ratios of the mineraliser to urea and the temperatures used for synthetising each morphology of $YbFeO_3$ are reported.

Morphology	KOH/ Urea Ratio [mol/mol]	Temperature [°C]	Dwell Time [h]
Cuboids	8.6	200-220	72
Elongated	7.0	200-220	72
Bipyramids	7.5	220-230	72

Table 2. Experimental parameters for the synthesis of each morphology of $YbFeO_3$.

5.3 Hydrothermal Synthesis of Co-doped $YbFeO_3$

For the synthesis of Yb ferrite doped with cobalt, two aqueous solutions were prepared, both with a 0.4 M concentration, one of $Yb(NO_3)_3$ (95% for non-stoichiometric $Yb_{0.95}Fe_{0.95}Co_{0.05}O_3$ and 100% for stoichiometric $YbFe_{0.95}Co_{0.05}O_3$) and the other consisting of 95% $Fe(NO_3)_3$ and 5% $Co(NO_3)_3$. The experimental procedure followed is the same as that described in the case of the synthesis of pure $YbFeO_3$ particles.

5.3.1 Hydrothermal Synthesis of $YbFe_{0.95}Co_{0.05}O_3$ at different KOH to urea molar ratios

Based on the results of the microparticle synthesis of $YbFe_{0.95}Co_{0.05}O_3$ (see Section 7.4 and 7.5 Results and Discussion Chapter), three synthesis series were carried out. In the first two series, the amount of urea added was varied while keeping the amount of KOH constant. The variation was 0.05 g (8.32×10^{-4} mol) per addition (up to a maximum of 0.50 g, 8.33×10^{-3} mol). While the third series consisted of varying the quantity of KOH at constant urea amount, with variations of 1.00 g of KOH (1.80×10^{-2} mol) between each addition (up to a maximum of 5.00 g, 9.07×10^{-2} mol).

In Table 3, 4 and 5 the moles and the KOH/urea molar ratios used for each of the three series are summarised. All the syntheses were carried out following the procedure described in Section 5.2, at 200 °C for 72 hours.

KOH [mol]	Urea [mol]	KOH/ Urea Ratio [mol/mol]
3.56×10^{-2}	4.16×10^{-3}	8.54
3.56×10^{-2}	5.00×10^{-3}	7.12
3.56×10^{-2}	5.83×10^{-3}	6.10
3.56×10^{-2}	6.66×10^{-3}	5.34
3.56×10^{-2}	7.49×10^{-3}	4.75

Table 3. Serie 1, variation of urea amount by keeping KOH constant.

KOH [mol]	Urea [mol]	KOH/ Urea Ratio [mol/mol]
5.08×10^{-2}	5.00×10^{-3}	10.17
5.08×10^{-2}	5.83×10^{-3}	8.72
5.08×10^{-2}	6.66×10^{-3}	7.63
5.08×10^{-2}	7.49×10^{-3}	6.78
5.08×10^{-2}	8.33×10^{-3}	6.10

Table 4. Serie 2, variation of urea amount by keeping KOH constant.

KOH [mol]	Urea [mol]	KOH/ Urea Ratio [mol/mol]
3.56×10^{-2}	5.00×10^{-3}	7.12
5.44×10^{-2}	5.00×10^{-3}	10.90
7.26×10^{-2}	5.00×10^{-3}	14.53
9.07×10^{-2}	5.00×10^{-3}	18.17

Table 5. Variation of KOH amount by keeping urea constant.

5.4 Reduction/Exsolution Treatments

The reduction/exsolution treatments of the prepared perovskite oxide powders were carried out weighing 0.05 g of the sample and placing it in a U-shaped quartz tube. The tube was connected to the gas flow (5% H_2/N_2) and to the mass spectrometer and placed into the oven. Firstly, the gas was let flow into the quartz tube at room temperature until it stabilised, then the heating program started with a ramping rate of 10 °C min^{-1} to reach the target temperature with a dwell time of 30 minutes, 1 hour or 5 hours. After the treatment the sample was quickly cooled down with compressed air keeping the gas flowing, afterwards the tube was taken down from the set-up and the powder was transferred into a glass vial. The samples were characterised by X-ray powder diffractometry (P-XRD), scanning electron microscopy (SEM), mass spectrometry (MS), and X-ray absorption near edge spectroscopy (XANES). Table 6 lists the reduction and exsolution treatments, carried out on various samples of the ferrite hydrothermally synthetised, with their temperature and residence time details.

Sample		Treatment	
Morphology	**Formula**	**Temperature [°C]**	**Dwelling Time**
Cuboids	$YbFeO_3$	900	30 minutes
		700	
		600	
		550	
		500	
		500	1 hour
Cuboids	$Yb_{0.95}Fe_{0.95}Co_{0.05}O_3$	550	30 minutes
		500	
		500	1 hour
		500	5 hours
Elongated	$YbFe_{0.95}Co_{0.05}O_3$	550	30 minutes
		500	
Bipyramids	$YbFe_{0.95}Co_{0.05}O_3$	550	30 minutes
		500	

Table 6. Reduction and Exsolution treatments carried out on various samples.

6 Characterisation methods

In the following section, the characterisation methods used in this work are reported and briefly discussed. The characterisation methods that will be discussed were useful for characterising the synthesised and heat-treated $YbFeO_3$ microparticles. In particular, the crystal structure and the crystalline phases constituting the microparticles were determined by powder X-ray diffraction (P-XRD); the morphology was determined by scanning electron microscopy (SEM); the reduction of the material during heat treatments was followed by mass spectrometry (MS); finally, X-ray absorption spectroscopy analyses (XAS) allowed a more in-depth analysis of the composition, coordination and electronic structure of the elements in the microparticles before and after the reduction heat treatment.

6.1 Powder X-Ray Diffraction (P-XRD)

Each crystalline solid has its own characteristic X-Ray diffraction pattern that can be used for its identification [85]. X-ray powder diffraction is a non-destructive technique based on the interaction of electromagnetic radiation with periodic structures having interatomic distances congruent with the wavelength of the incident X-rays. During a PXRD measurement, a crystalline sample is irradiated by an X-ray beam, which is scattered, or diffracted, by the atomic planes of the crystal; the scattered radiation gives rise to constructive interference (diffraction maximum) when Bragg's law is satisfied [86]:

$$2d_{hkl}sin\theta = n\lambda$$

Where d_{hkl} is the distance between parallel reticular planes (*hkl*), θ is the angle of incidence of the radiation, n is the diffraction order and λ is the wavelength of the incident radiation. The positions of the reflections in the diffractogram are thus inversely related to the distances between the planes generating them. In a powder sample, the

various lattice planes are present in every possible orientation. Therefore, for each set of planes, some crystals are always oriented at a Bragg angle (θ) with respect to the incident beam and thus diffraction occurs for these planes.

Converting diffraction peaks into d-spaces via the Bragg equation allows the compound to be identified, as each has a unique set of d-spaces that act as a "fingerprint". This can be done by comparing the d-spaces of the compound with standard reference [87].

In addition, reflection intensities can be related to particle morphologies [88,89]. The larger a crystalline plane is, the more atoms reflect X-rays, so that a higher intensity is detected [90]. However, the connection is not clear, because the reflection intensities, especially in the case of anisotropic particles, also depend on the orientation of the particles during X-ray diffractometry. Consequently, different measurements of the same sample can lead to different reflection intensities [89]. Furthermore, the reflection intensities are determined by the electronic densities of the individual atoms. This is particularly important for doped samples in which the reflections of the product and the dopant are at similar angles.

Powder X-ray diffractograms were recorded at room temperature in theta-theta geometry with $Cu_{K\alpha1}$ radiation of 1.5406 Å wavelength, with a 45 kV, 40 mA,using an *X'Pert Pro MPD* from *PANalytical*. The measurement time was 500 s per 724 steps at a step width of 0.013° 2θ in the range of 0.5–10° 2θ. The evaluation of the powder X-ray diffractograms was carried out using the Match! software package.

6.2 Scanning Electron Microscopy (SEM)

The scanning electron microscope (SEM) can be used to visualise structures of objects smaller than 1 µm that are no longer accessible with conventional microscopy. With it, surfaces with resolutions down to 1 nm can be visualised. For this purpose, an electron beam is used, which is generated by a thermal or field emitter and then accelerated and focused on the sample to be analysed. A high energy electron beam is used to irradiate the sample and the outcoming electrons/X-rays are analysed. The outcome beam is used to visualise surface images of a material. SEM provides qualitative

information about the surface features, shape, size and arrangement of the sample's surface [91].

The measurement chamber of the sample is under high to ultra-high vacuum conditions to avoid any interference during the measure. When the electron beam irradiates the sample, it interacts with the primary electrons (PE) resulting in elastic or inelastic scattering. Elastic scattering involves small variations in energy, but sometimes significant directional shifts due to interactions with sample's atomic nucleus and electron shell. In inelastic scattering, excitation or ejection events occur involving plasmons, phonons or valence electrons, sometimes leading to the emission of characteristic X-rays. Imaging is based on the emitted electrons, mainly secondary electrons (SE) and backscattered electrons (BE). The contrast of the image depends on the number of SEs emerging from the sample, while BEs come from deeper layers and reveal the composition of the material based on the atomic number of the atoms [92].

To study the morphology of the prepared samples, Scanning Electron Microscopy (SEM) images were obtained on a LEO1550 operating at 2.00 kV. The powder was fixed on a standard carbon conductive tab and was investigated without further conductive coating.

6.3 Mass Spectrometry (MS)

Mass Spectrometry is an analytical method characterised by excellent sensitivity, high detection limits, speed and versatility. Mass spectrometry is based on the vacuum separation of ions in the gas phase according to their mass-to-charge ratio (m/z). A high-energy electron beam (e^-), produced by passing a current through a filament (usually tungsten), is directed towards the substance of interest, M. The electron beam is sufficiently energetic to cause the removal of an external electron from M, thus producing a radical-ion, M^+. The ionisation process can be described by the following equation:

$$M + e^- \rightarrow M^{\cdot +} + 2e^-$$

The produced molecular ion usually undergoes some further fragmentations due to high energy level imparted to the ion-radical. The ions enter a mass analyser where they are subjected to electromagnetic forces that determine their separation according to their mass-to-charge ratio (m/z). The process described above involves a chemical reaction between the substance of interest, M, and an electron, e-, followed by further non-reversible dissociation reactions. It derives that mass spectrometry is a destructive method of analysis. Fortunately, the technique is very sensitive and only a small amount of material is required to perform an analysis [93]. This analysis provides a mass spectrum as plot of ion abundance versus the mass to charge ratio. The most intense peak is called base peak and is assigned the relative abundance of 100% with the others being normalised to it.

6.4 Temperature Programmed Reduction by Hydrogen

Temperature Programmed Reduction by H_2 (TPR−H_2) is a sensitive technique based on probing the material surface as a function of temperature in a controlled atmosphere. It is particularly relevant to obtain qualitative information about the reducibility of different components on a oxide catalyst [94]. In a typical TPR- H_2 run, the catalyst is placed in a reactor, heated under a reducing gas flow, typically H_2 diluted in Ar or N_2. The temperature is increased at a linear heating rate. The set-up includes a mass spectrometer to monitor the change in the gas stream. When a reduction of the sample occurs, H_2 is consumed. The amount of hydrogen consumption with increasing temperature gives a measure of the reducibility of the material.

Since the exsolution process involves the reduction of host oxides [95], the use of mass spectrometry during the TPR−H_2 treatment is one of the most common techniques to follow the exsolution process of a metal. Here the evolution of the water signal is followed and gives important insights about the release of lattice oxygen and thus the reduction of the metal [96]:

$$M^{n+} + ne^- \rightarrow M^0$$

$$H_2 + O^{2-} \rightarrow H_2O + 2e^-$$

Exsolution treatments of the perovskite oxide powders were carried out in a U-shaped quartz tube with a 4 mm diameter and coupled with a Cirrus2 MKS mass spectrometer. 5% H_2/N_2 (volume ratio 5/95) was chosen as reducing atmosphere with a flow rate of 1.2 $l \cdot h^{-1}$. The samples were heated with a ramp of 10 $°C \cdot min^{-1}$ up to the target temperatures and kept there for 30 minutes, 1 hour or 5 hours before cooling down to room temperature.

6.5 X-Ray Absorption Spectroscopy

X-ray spectroscopy is a powerful analytical technique that uses X-rays to excite core electrons (in the s or p shells) in a molecule or material due to their high energies (500 eV to 2000 keV). This method offers intrinsic element specificity, allowing the measurement of a single element within a complex matrix. X-ray spectroscopy is bulk sensitive and versatile, it is very flexible in terms of the types of materials and systems that can be studied. Rapid data collection enables time-resolved experiments and provides unique chemical insights [97].

In X-ray spectroscopy, light is absorbed through the photo-electric effect [98]. Photons excite core electrons in unoccupied orbitals of higher energy, producing a spectrum divided into three regions (Figure 7). The “pre-edge” corresponds to the excitation of core electrons in bound orbitals, while the “edge transition” occurs at higher energy levels as a consequence of electron ionisation. Beyond that, at even higher energies, there is Extended X-ray Absorption Fine Structure (EXAFS) region characterised by little wiggles. Edges are named based on the origin of the electron being excited: electrons excited from the n=1 shell are K-edges; from the n=2 shell are L-edges etc. (Figure 8). The edge energy increases with the atomic number of the element [99], and each element has absorption edges at unique energies that can be selectively probed by XAS, that is why it is an element-selective technique [98]. At most

X-ray energies, the absorption coefficient μ has a strong dependence on atomic number Z and energy E, according to this formula:

$$\mu \approx \frac{\rho Z^4}{AE^3}$$

where ρ is the sample density, and A the atomic mass.

Like many of absorption type spectroscopies, XAS is governed by the dipole selection rule. Since the photon has angular momentum (*l*) of 1, the electron on the absorbing atom must undergo Δ*l* = ± 1 in order to conserve the momentum. As each orbital possesses its own angular momentum, only specific electron transitions are allowed. For example, an electron from the s-level (*l* = 0) can be excited into an empty p orbital (*l* = 1) [100].

The prominent edge peak provides information about the oxidation state of the absorbing atom. As the oxidation state increases, the edge energy tends to increase, making edges valuable probes for oxidation state information. The shape of the edge spectrum is influenced, inter alia, by the ligands binding to the metal, and the scattering of the photoelectron during ionisation is also important. Heavier atoms tend to shift the edge to lower energies. The energy of the edge represents the difference between the 1s orbital and the continuum (ionised state), so any factor affecting the energy of the 1s orbital will have an impact the edge energy [98]. In addition, XAS spectra include lower intensity peaks from electron transitions from 1s to 3d orbitals that follow the quadrupole selection rule (Δ*l* = ± 2) [97]. These pre-edges transitions are typically weaker than dipole allowed. They offer valuable information on the oxidation state of the absorbing atom from both the energy and the intensity. The energy and intensity tend to increase with increasing oxidation state (due to more empty d orbitals and more covalency between metal and ligand, so more p-d mixing is possible). Pre-edges can also provide information on the symmetry of the absorbing atom, which results from the mixing between p and d orbitals promoted by certain symmetries (e.g., shorter metal-ligand bonds favour p-d mixing) [97].

To transform XAS data into useful information, a three-step process is followed: data processing for interpretation, fitting to deconvolve spectra into discrete peaks and

collect rigorous statistics, and analysis to extract chemically relevant information, such as oxidation state and coordination geometry [98]. XAS data can be collected in two main modes: transmission mode, in which the X-rays detected are those passing through the sample, and fluorescence mode, in which the fluorescence emitted by the sample is monitored [101]. Multiple spectra are often collected on the same sample to improve the signal-to-noise ratio, and the intensity axis must be consistent to compare spectra from different samples.

The XAS experiments were performed at the beamline P64 of PETRA III at DESY, Hamburg.

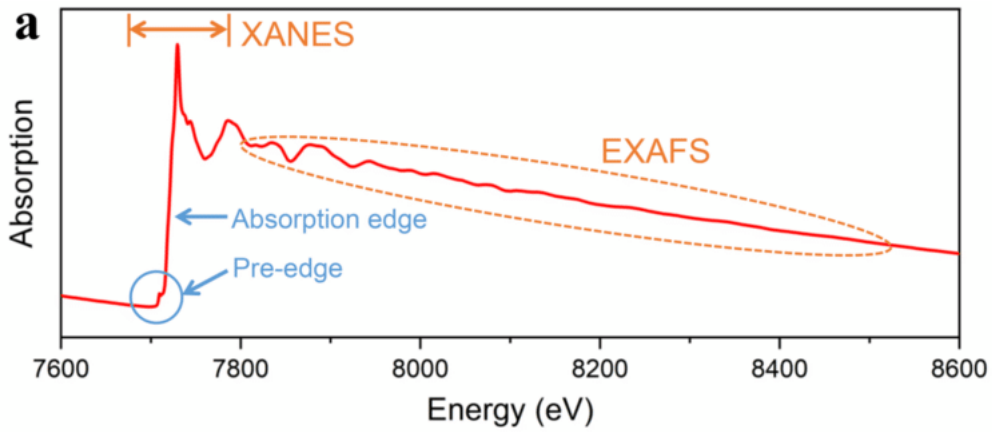

Figure 7.Example of a XAS spectrum divided in its three main regions [101].

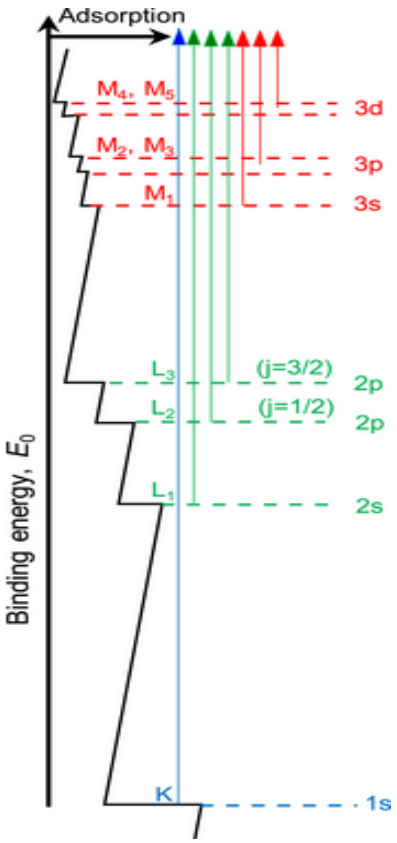

Figure 8. Possible transitions of the electrons during a XAS measurement and their labelling [102].

7 Results and discussion

7.1 Hydrothermal synthesis of $YbFeO_3$

Firstly, the pure $YbFeO_3$ was synthetised via the hydrothermal route following the procedure described in Chapter 5. In the following section the results from the synthesis of three samples, which differs for the molar ratio of KOH and urea used and for the temperature treatment, are reported and discussed. The material was analysed by scanning electron microscopy (SEM) and powder X-ray diffraction (P-XRD).

The product obtained was a dark red powder composed of particles in the micrometre size range (Figure 9). Cuboids presented edges of approximately 8 μm; elongated tetragons of 17 and 6 μm; bipyramids of 11 μm (major base of the pyramid) 4 μm (minor base of the pyramid) and 8 μm (lateral edges). The XRD patterns, shown in Figure 10, revealed that each sample is mainly composed of a $YbFeO_3$ phase [103]. However, the presence of a small reflection peak, around 35.5 2θ [°], showed the presence of a secondary phase of Fe_2O_3 [104] ascribed as an impurity. No ytterbium oxide signal was observed. This suggests that all the Yb in the reaction mixture was incorporated into the final perovskite matrix, resulting in a non-stoichiometric ferrite with an excess of Yb. Alternatively, it is possible that the remaining Yb was present in the sample as an amorphous phase or in such a minimal amount that the instrument could not detect it. By indexing of the XRD data, and by the matching of the reflection positions, it could be stated that all the samples of $YbFeO_3$ product coincide with those of the orthorhombic space group *Pbnm* [105].

From the SEM images of the three samples (Figure 9), the crucial role of the KOH/urea molar ratio in the hydrothermal formation of metal oxide crystals was observed. Cuboid-shaped $YbFeO_3$ microparticles were obtained with a KOH/urea molar ratio of 8.6, at 200 °C for 72 hours (Figure 9 (a)). Decreasing the ratio to 7.0 led to tetragonal elongated morphologies (Figure 9 (b)), at the same temperature condition as the cuboids. The bipyramidal microparticles required a higher temperature, 220 °C, and a

KOH/urea molar ratio of 7.5 (Figure 9 (c)). The experimental parameters are summarised in Table 2 (Chapter 5.2).

Particles with different morphologies are characterised by different sets of crystalline facets. These differences, in addition to SEM analysis, can be detected by an XRD analysis as they lead to different reflection intensities in the XRD pattern [106]. Here, the predominant facets were {110}, {002}, {111}, {020}, {112}, {200} and {220} with different ratios and combinations depending on the morphology (Figure 10). The reflections from the {110} and the {220} facet are especially pronounced for the elongated tetragons, while the {020} and {112} are more exposed for the bipyramids and the cuboids. From these analyses, it was possible to confirm the successful synthesis of $YbFeO_3$ microparticles with the three morphologies of interest. Varying the KOH/urea molar ratio, different crystal facets grow. This is due to the stabilising effect of the ions in solution (K^+ and NH_4^+) on the different facets during crystal growth. By varying the concentration of these ions in solution, microparticles with different shapes were obtained.

SEM analysis showed that the microparticles of $YbFeO_3$ exhibit a certain degree of surface defects such as cracks, holes and dislocations along the edges. In the cuboid sample, many multiple growth particles were present as if the particles were embedded in each other. All these defects could be caused by incomplete or failed crystal formation during the hydrothermal process [107–109] In addition, smaller amorphous particles of a lighter colour than the microparticles of $YbFeO_3$ were visible around the crystals. When a colour contrast is observed in SEM images, it can be assumed that the chemical compositions are different, so the amorphous particles were probably impurities.

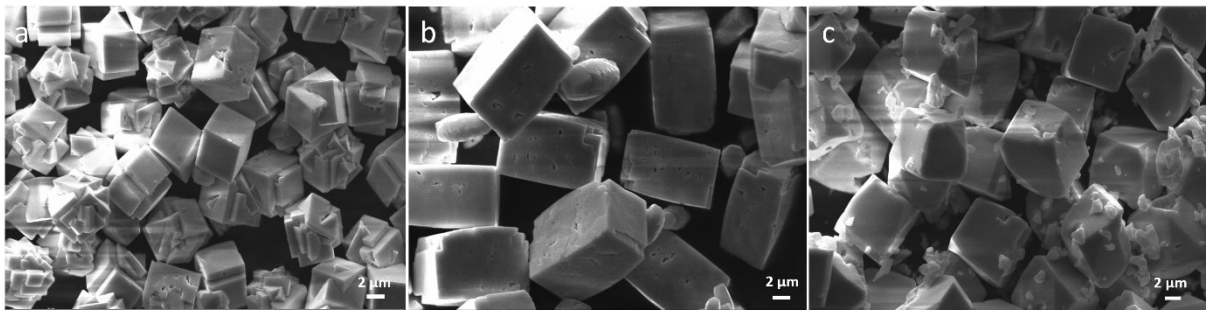

Figure 9. SEM images of the three different morphologies of $YbFeO_3$ microparticles: (a) Cuboids (b) Elongated Tetragons (c) Bipyramids.

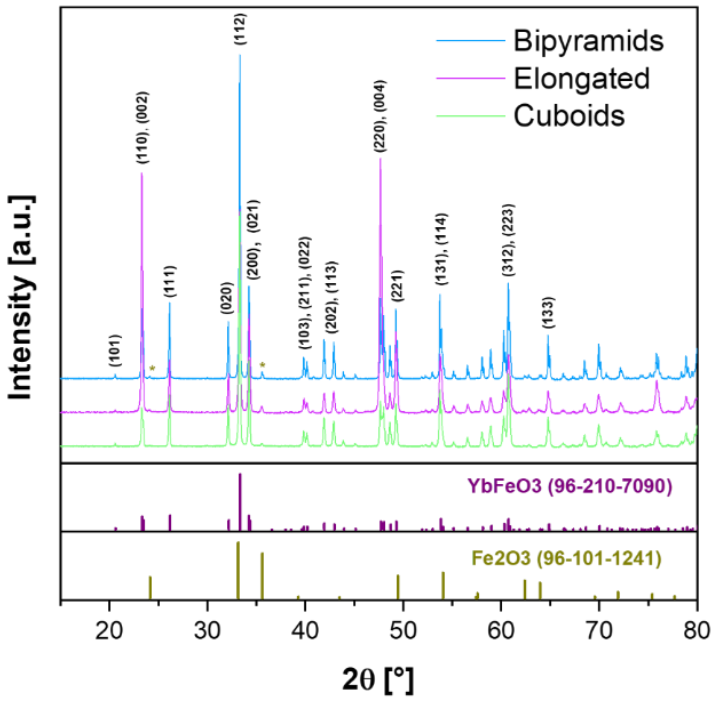

Figure 10. XRD patterns of the three different $YbFeO_3$ microparticles with Miller indexes.

7.1.1 Effect of the Temperature on the synthesis of $YbFeO_3$

Since the previous results showed a certain degree of iron oxide impurities and a coarse particle morphology, higher temperatures of hydrothermal treatment were explored in the attempt to improve the synthesis results. The cuboids and the elongated tetragons were treated at 220 °C while the bipyramids at 230 °C, maximum temperature attainable from the oven used. The synthetic procedure and quantities of reagents used did not vary from those employed in the previous synthesis. SEM analysis of the three dark red powders (Figure 11) showed that the particles obtained were still in the micrometre size range and with similar sizes of the previous sample, so the temperature did not affect the size distribution. However, a change in shape could be observed, which is preferentially of the bipyramidal type (Figure 11 (a)). This change was also observed in the change in the intensity of the reflections of the XRD pattern (Figure 12), compared to the samples discussed above. In particular, one can see the decrease in the reflection relative to planes {110} and {220}, which were particularly pronounced due to the morphology of the elongated tetragons. In addition, upon the synthesis at higher temperatures, the main reflexes of all three samples showed comparable intensities in

favour of the microparticles having a similar shape. In all samples, amorphous material was clearly visible around the microparticles, which also exhibit a large number of surface defects, steps along the edges and agglomerations. From the XRD graphs, the main phase was $YbFeO_3$ with an orthorhombic crystal system [103], however, a secondary hematite phase was still present [104]. As in the previous synthesis, no ytterbium oxide signal was observed. Therefore, the same considerations regarding the formation of a $YbFeO_3$ with excess Yb or the non-detection of the Yb oxide phase by the instrument could be made. These results therefore confirmed that the hydrothermal synthesis of $YbFeO_3$ at temperatures above 230 °C did not lead to an improvement of the material either in terms of purity or particle morphology.

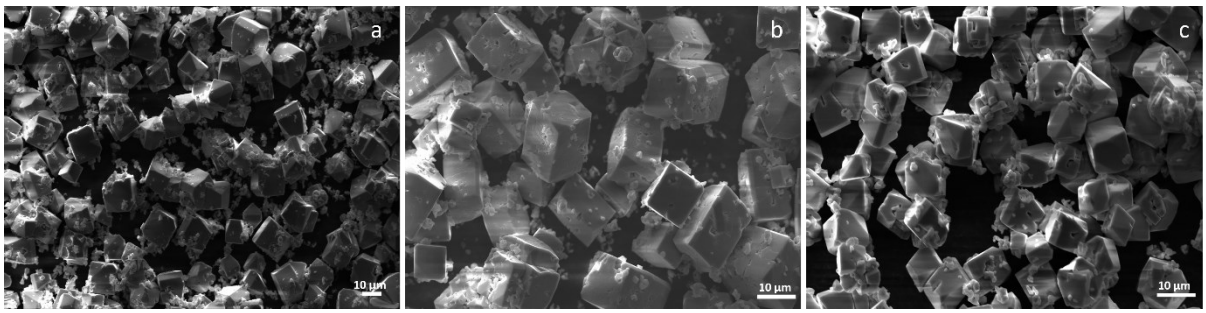

Figure 11. SEM images of the three different morphologies of $YbFeO_3$ microparticles after the treatment at higher temperature: (a) Cuboids (220 °C) (b) Elongated Tetragons (220 °C) (c) Bipyramids (230 °C).

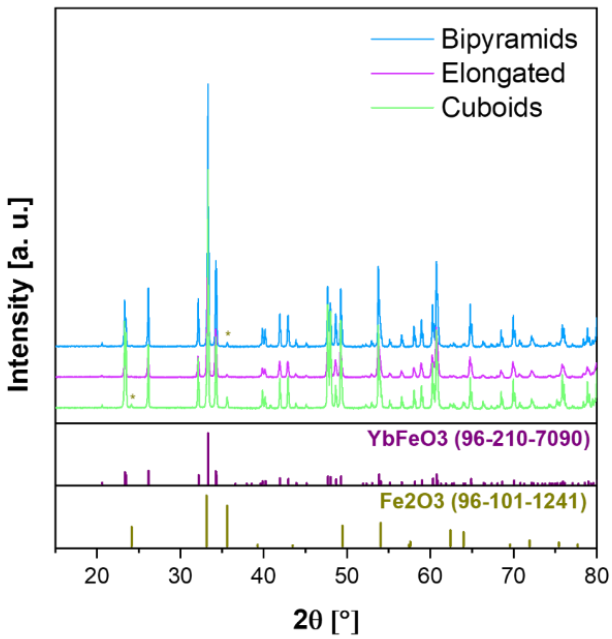

Figure 12. XRD patterns of the three different $YbFeO_3$ microparticles after the synthesis at higher temperatures.

7.2 Doping with Cobalt: Hydrothermal synthesis of $Yb_{0.95}Fe_{0.95}Co_{0.05}O_3$

Having demonstrated the reproducibility of the synthesis of $YbFeO_3$ microparticles, the material was doped with 5% w/w cobalt. The synthetic procedure, the amounts of reagents used and the reaction conditions to synthesise the desired material were the same as those used in the case of $YbFeO_3$ particles and are summarised in Chapter 5.3.

The synthesised material was intended to be used as a matrix for the exsolution of metal nanoparticles. Since it is well known that this process is favoured by the deficiency of A-sites in the primitive oxide lattice [110], the synthesis carried out initially was that of non-stoichiometric $Yb_{0.95}Fe_{0.95}Co_{0.05}O_3$.

The product obtained was a red-brown powder, the change in the colour between undoped and doped $YbFeO_3$ could be a first confirmation of the change in the chemical nature of the material.

In Figure 13 can be seen that the powders obtained were composed of microparticles of different morphologies. The cuboids and the bipyramids samples were similar to their undoped counterparts, with the same characteristics of shape, size, particle defects and agglomerations. In contrast, a large amount of amorphous material was visible in the elongated tetragon sample. The evaluation of the crystalline structure via X-ray diffractometry shown that all the samples were composed mainly of orthorhombic $YbFeO_3$ with the space group *Pbnm*, but impurities of Fe_2O_3 persisted. In the elongated tetragons, a third YbO(OH) phase was also observed. In none of the samples signals of a cobalt oxide phase [111] were visible, suggesting that the dopant was incorporated into the ferrite crystal lattice.

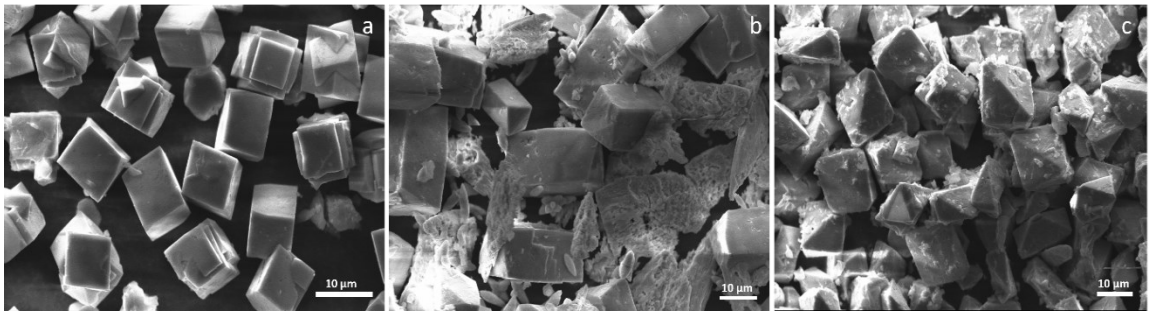

Figure 13. SEM images of the three different morphologies of Co-doped $Yb_{0.95}Fe_{0.95}Co_{0.05}O_3$ microparticles: (a) Cuboids (b) Elongated Tetragons (c) Bipyramids.

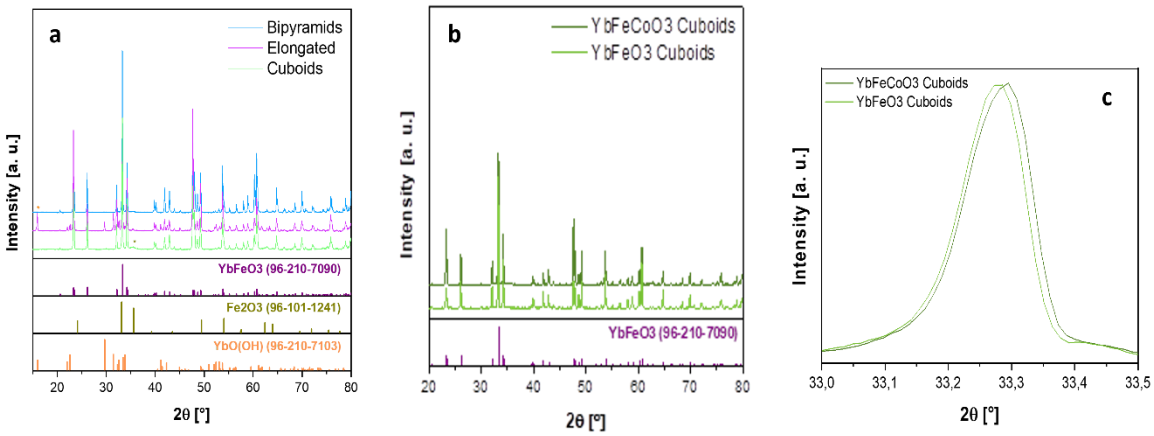

Figure 14. (a) XRD patterns of the three different morphologies of the Co-doped $Yb_{0.95}Fe_{0.95}Co_{0.05}O_3$ microparticles; (b) XRD patterns of the undoped $YbFeO_3$ and of the Co-doped $YbFeCoO_3$ with cuboidal morphology; (c) shift of the perovskite most intense reflection for the cuboidal morphology.

A comparison of the XRD patterns of $YbFeO_3$ and $Yb_{0.95}Fe_{0.95}Co_{0.05}O_3$ samples might give some indication of the successful incorporation of Co into the perovskite matrix. Since the doping involves a substitution of certain Fe^{3+} cation sites with Co^{3+}, the lattice parameters of $YbFeO_3$ are altered and this causes a shift of the reflections in the XRD pattern. The ionic radii of Co^{3+} (0.61 Å) is smaller than that of Fe^{3+} (0.64 Å) [73], so the unit cell of $Yb_{0.95}Fe_{0.95}Co_{0.05}O_3$ shrinks [112]. Since the distance between the crystalline plane is smaller, the diffraction angle will be greater (shift toward higher 2θ values), in accordance with Bragg´s law. This evolution was visible only for the cuboid sample and is shown in Figure 14 (c). This could suggest that the chemical composition of the material, following the incorporation of the dopant into the B-sites of the perovskite matrix, changed only in this sample. While in the case of the other morphologies, the product obtained either contains no Co, or Co was present in such low amounts that it did not cause significant changes in the crystal structure. However, the shift is minimal, and it was difficult to say whether it was really due to the shrinkage of the lattice constant as a result of the Co incorporated in the $YbFeO_3$. Nonetheless, in the XRD analysis there was no evidence about the formation of any cobalt oxide phase (CoO, Co_3O_4). At this point, it should be mentioned that the formation of Co_2O_3 is unlikely as this oxide was only reported at extremely high pressures (≥ 90 kbar) and temperatures (1000 °C) exceeding the conditions of the applied hydrothermal synthesis [113]. For this reason, it will not be included in further discussion. The lack of signals related to any

cobalt oxide phase could be a consequence of different factors, or a combination of them. Firstly, the XRD is a quantitative analysis in which the results depend also on the amount of sample used, particularly when the sample size is very small or when the material is inhomogeneous. Here the dopant was present in a very small quantity (5% w/w) which means a small crystalline volume fraction of the phase [114], and therefore it could be that the number of scattering centres were not enough to provide a signal detectable by the instrument. In addition, the signal from Co could not be observed due to the high intensity of the perovskite reflections. Another reason could be due to the structure of the CoO: if it was present as an amorphous compound, it would not produce any signal in the XRD pattern.

To shed light on the local structure and chemical environment of the dopant in the material, XAS analysis at the Co K-edge (E_{Co} = 7709 eV) on the sample of the cuboids was carried out. The normalized XANES and its first-order derivative are reported in Figure 15.

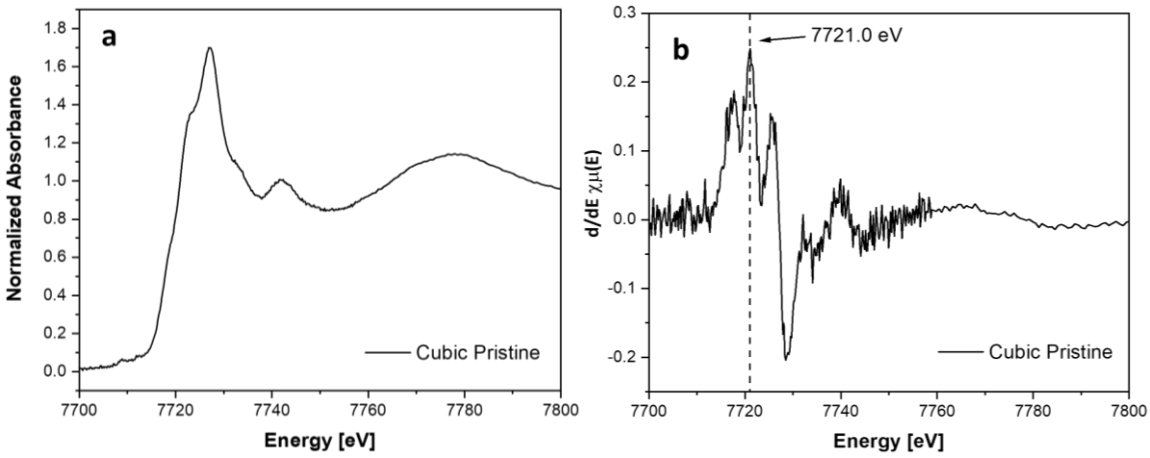

Figure 15: (a) Normalized XANES spectra and (b) first-order derivative of XANES Co K-edge in Co-doped non-stoichiometric cuboids microparticles of $Yb_{0.95}Fe_{0.95}Co_{0.05}O_3$.

The obtained XANES spectrum is characterised by a main absorption peak at 7728 eV that presents two shoulders: one on the low energy flank, around 7723 eV, and the other on its right side at the energy of 7734 eV. These results are compared with a cobalt oxide references (CoO, Co_3O_4) from the literature [115]. Both, the shape and the characteristic (main peak and shoulders positions) of the XANES spectra coincide with that of CoO. In support of this there is the shape of the first derivative of the XANES

which is identical to the one of CoO excluding other chemical environments around the cobalt absorber, e.g. Co_3O_4. The edge energy of the most intense peak is 7721.0 eV, slightly lower than that of Co^{2+} (7722.5 eV) of the reference. The edge position suggests an average oxidation state (*n*) lower than +2, which is not reasonable for Co. This small difference in the energies (1.5 eV) could be due to a non-perfect normalisation of the XANES spectrum here reported. From this analysis there is a reason to believe that Co^{3+} was not incorporated into the perovskite B-site ($^{oct}Co^{n+}$) but was present in the sample as Co^{2+}, in particular as CoO. Furthermore, the possible formation of a spinel phase ($CoFe_2O_4$) was investigated. In this regard, the comparison was based on the Fe K-edge spectrum (Figure 36) of pristine doped $Yb_{0.95}Fe_{0.95}Co_{0.05}O_3$ and revealed a lower energy of the absorption edge (7130 eV) as compared to spinel oxide (7135 eV) ruling out the formation of this phase [116]. It is reasonable to assume that the analysis of the results made on this sample is also representative for the other morphologies since the crystalline structure was identical for all the samples as well as the synthesis conditions.

7.2.1 Effect of the Temperature on the synthesis of $Yb_{0.95}Fe_{0.95}Co_{0.05}O_3$

The effect of higher temperatures was also explored in the case of the synthesis of $Yb_{0.95}Fe_{0.95}Co_{0.05}O_3$ microparticles: 220 °C was the treatment for the cuboids and the elongated tetragons batches, while 230 °C for the bipyramids. SEM images and XRD are reported in Figure 16 and 17 respectively. It seemed that the obtained powders were formed by orthorhombic $YbFeO_3$ with no significant impurities. As observed in the case of the pure ferrite, higher temperatures led to the generation of bipyramidal microparticles. In the case of the bipyramids (Figure 16 (c)) and the cuboids samples (Figure 16 (a)), the presence of many non-uniform morphologies, clusters and agglomerations, not present in the case of elongated tetragons, were visible. For the last-mentioned sample, the particles had a bipyramidal elongated shape. Cracks, holes and uncomplete edges were still present on the surfaces of the particles. XRD results showed that the hydrothermal synthesis of $Yb_{0.95}Fe_{0.95}Co_{0.05}O_3$ at higher temperatures apparently led to a purer product. SEM analysis, however, showed that there was no

definite morphology (Figure 16 (a) and (c)), and the elongated particles were no longer tetragons but more “rectangular” bipyramids.

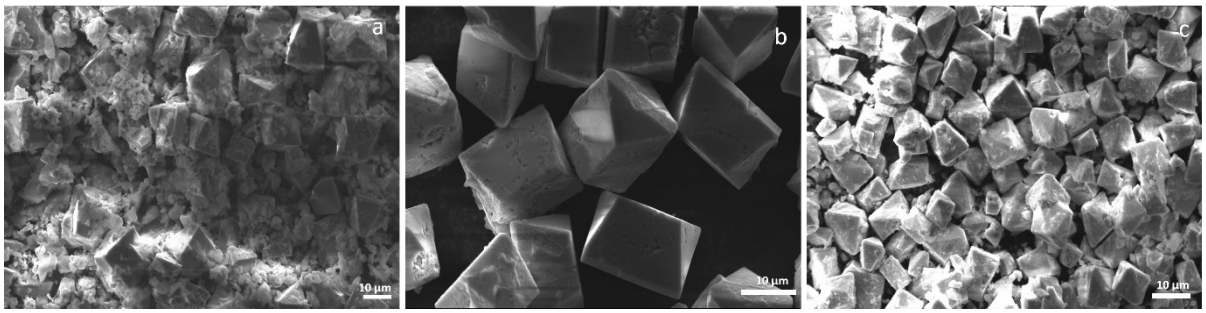

Figure 16. SEM images of the three different morphologies of $Yb_{0.95}Fe_{0.95}Co_{0.05}O_3$ microparticles after the treatment at higher temperature: (a) Cuboids (220 °C) (b) Elongated Tetragons (220 °C) (c) Bipyramids (230 °C).

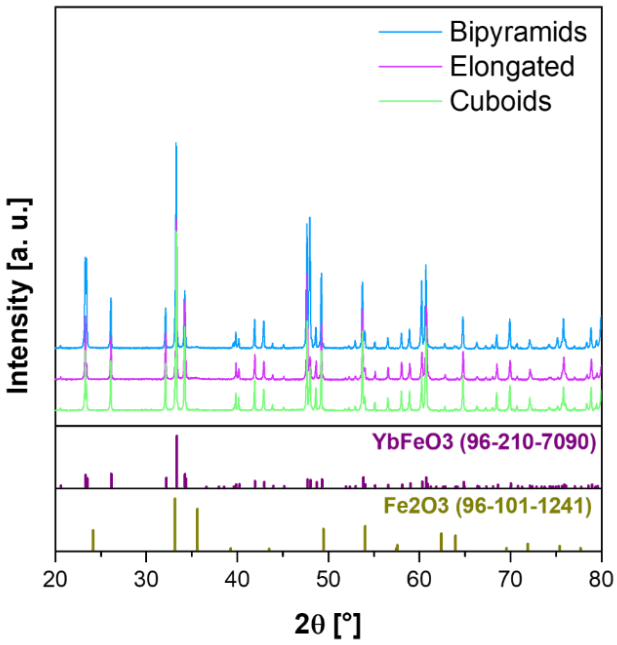

Figure 17. XRD patterns of the three different $Yb_{0.95}Fe_{0.95}Co_{0.05}O_3$ microparticles after the synthesis at higher temperatures.

7.3 Relationship between iron oxide impurities and hydrothermal synthesis

Hydrothermal synthesis is very sensitive to several parameters such as temperature, solvent, pH, residence time, nature and concentration of reagents, and presence of chelating agents. Even the slightest change in any of these parameters can alter the result of the synthesis. The exact mechanism that leads to the formation of oxide crystals during the hydrothermal process is not known [117]. The most popular theory is that the process is divided into an initial in-situ transformation stage followed by precipitation and growth. Initially, there is the dissolution of the precursors in the reaction mixture and the subsequent formation of the oxides and hydroxides from the combination of metal ions with the hydroxyl groups generated from the ionization of water at high temperature. Due to the low solubility of the final product in the liquid phase, the formation of nucleation crystals takes place, which act as seeds for crystal growth. The mineralizer acts as a catalyst for the dehydration reaction of the metal hydroxides, thus allowing the crystallisation process to take place at lower temperatures [118]. Zhou et al. performed the hydrothermal synthesis of multiferroic rare-earth orthoferrites, proposing a dissolution-precipitation mechanism for the formation and growth of $REFeO_3$ [41]. The result of this synthesis really depends on the kinetics of the two phases: when precipitation occurs at slow rate, it leads to the formation of a single large crystal. Conversely, if the solute precipitates rapidly, the kinetics of crystal seed formation (nucleation) will prevail over growth kinetics, resulting in the formation of numerous small crystals, typically with a narrow size distribution [119]. In the case of this work, basing on the previous statement, it can be assumed that the crystal seed formation had the faster kinetics, since the product was obtained as a fine powder. Furthermore, based on the results obtained, it could be said that hydrothermal synthesis under the employed conditions led to the formation of monodisperse single crystals with different morphologies depending on the KOH/urea molar ratio. A trend common to all the results reported so far was that the obtained microparticles presented many surface defects (holes, cracks, incomplete edges and angles) and the occurrence of secondary particles. Moreover, the final product was never completely pure but always co-exist with an impurity phase of Fe_2O_3. The first effect could be explained by

considering that the crystal formation process in hydrothermal synthesis results from complex and interplaying phenomena. It is likely that the defects observed are formed during these stages. The incomplete growth could lead to formation of pits and fragmented edges, while agglomerates could originate from competition between the dissolution-precipitation and nucleation mechanisms. Zhou and coworkers in their study about hydrothermal synthesis of $REFeO_3$, reported that also the alkalinity plays a crucial role in the formation of ferrites. The pH affects the solubility of the precursors: the concentration of the ions should give an ion product below the value of the solubility product constant (Kps), in order for the solution to remain unsaturated. If the concentration of OH^- groups in solution is too low the hydroxyl complexes will not form and the precipitation of crystalline Fe_2O_3 will occur after the hydrothermal treatment [41]. In the case of the synthesis of A-site deficient microparticles, with formula $Yb_{0.95}Fe_{0.95}Co_{0.05}O_3$, an excess of iron precursor was employed. An oxide structure with A-site deficiency is less stable, which means that it requires a higher energy for its formation than the stoichiometric equivalent. It could be assumed that the hydrothermal synthesis did not yield the A-site deficient system, and instead, the more stable stoichiometric system was formed. Thus, the incorporation of the excess iron into the crystal lattice of the perovskite does not occur, and it will react with the hydroxyl groups to form the corresponding oxide or hydroxide. Basing on this hypothesis, the synthesis of stoichiometric $YbFe_{0.95}Co_{0.05}O_3$ was carried out in an attempt to minimise the secondary phase in the target product.

The incomplete incorporation of Co into the perovskite host lattice could be a result of two factors. Firstly, the lack of dissolution of $Co(OH)_3$ as a hydroxyl complex (see reactions in Section 4.3, Hydrothermal synthesis). As hydroxides are amorphous solids, they are not detected by XRD measurements, and this would be in line with the fact that no secondary phase of Co was visible in the diffractograms of the doped samples. Added to this hypothesis is the assumption that pure $YbFeO_3$ was the most stable compound and therefore the only one formed under the hydrothermal conditions employed in this work.

7.4 Doping with Co: hydrothermal synthesis of $YbFe_{0.95}Co_{0.05}O_3$

The synthesis of stoichiometric $YbFe_{0.95}Co_{0.05}O_3$ was carried out following the same procedure used for the other samples. As observed for all the previous samples, the red-brown powder was composed of microparticles of orthorhombic $YbFeO_3$. The XRD patterns (Figure 19) revealed the existence of two additional phases, one composed of Fe_2O_3 and the other of YbO(OH) particularly evident in the cuboid and bipyramid samples. Notably, star-shaped particles could be observed in the SEM of the cuboid sample Figure 18 (a)), believed to be impurities. All the samples had the shape of bipyramids (Figure 18), slightly distorted for the cuboids batch. This was quite surprising since in the case of $Yb_{0.95}Fe_{0.95}Co_{0.05}O_3$ the three morphologies were achieved. Perhaps the different stoichiometry affected the stability of the individual crystalline facets, favouring those of bipyramidal morphology during the crystallisation process of the microparticles. An attempt was made to improve the cuboid sample by carrying out the synthesis in a 25 mL Teflon liner and leaving the reaction mixture under stirring for 1 hour after the addition of urea in order to achieve optimal homogeneity of the reagents. However, no improvement in product purity or morphology was obtained.

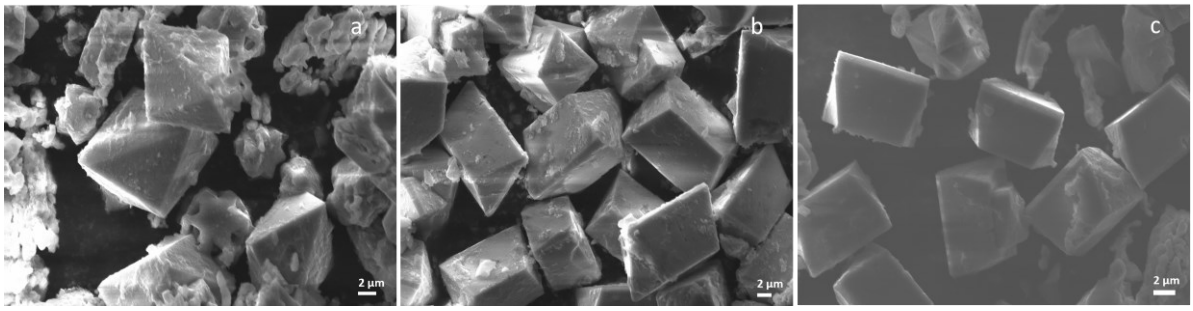

Figure 18. SEM images of the three different morphologies of stochiometric Co-doped $YbFe_{0.95}Co_{0.05}O_3$ microparticles: (a) Cuboids (b) Elongated Tetragons (c) Bipyramids.

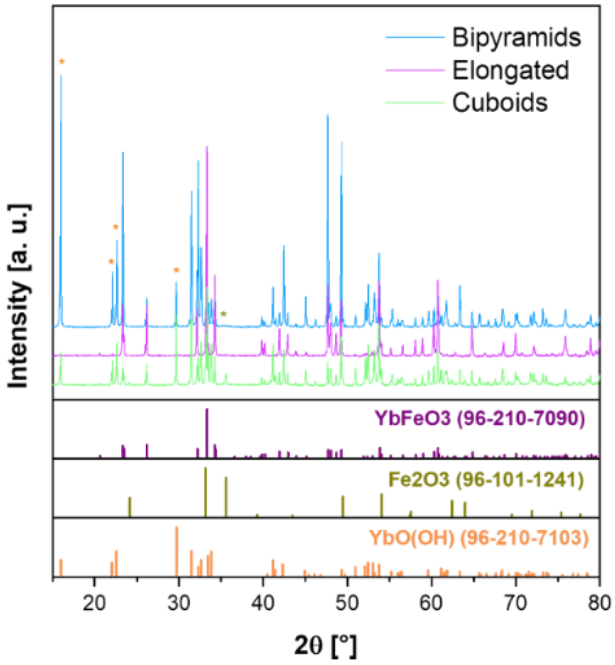

Figure 19. XRD patterns of the Co-doped $YbFe_{0.95}Co_{0.05}O_3$ microparticles with different morphologies.

7.5 Synthesis optimization

Since the results of the hydrothermal synthesis of the stoichiometric material did not lead to good quality microparticles and were not reproducible, it was decided to explore the effect of the KOH/urea molar ratio with the aim of trying to optimise the synthesis. In the following paragraphs are reported and discussed the results obtained by varying the amount of urea, with constant KOH, and vice versa.

7.5.1 Effect of urea in Hydrothermal synthesis of $YbFe_{0.95}Co_{0.05}O_3$

Firstly, the effect of urea was studied. Two series of syntheses were carried out in which the amount of urea added was varied while keeping the amount of KOH constant. The obtained material was analysed via SEM and XRD and the results are reported in Figure 20-21 and 22 respectively.

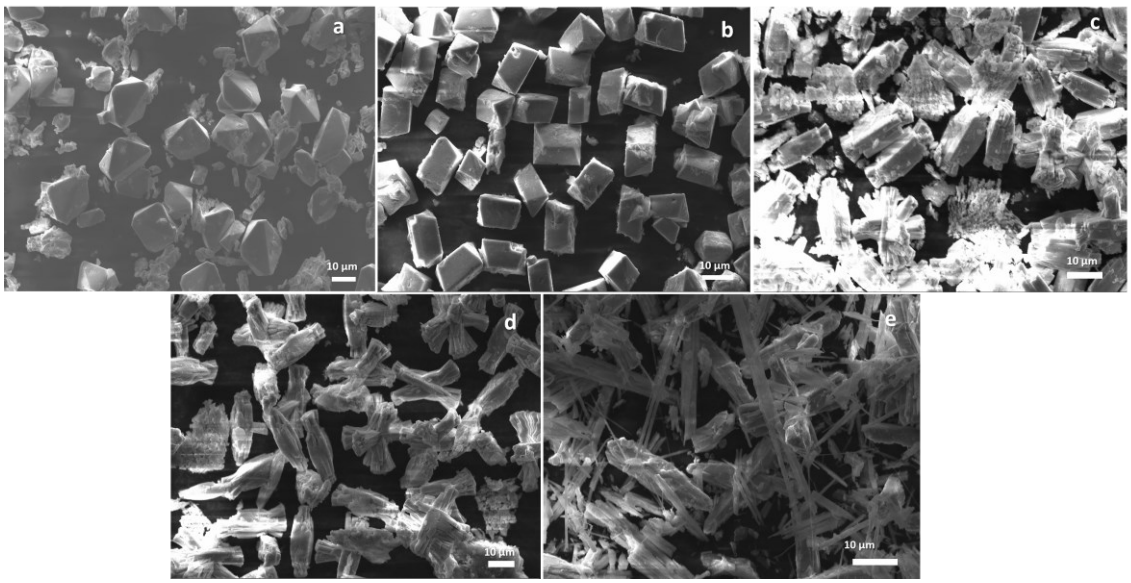

Figure 20. SEM images of the effect of the amount of KOH/urea molar ratio in Series 1: (a) KOH/urea 8.54 (b) KOH/urea 7.12 (c) KOH/urea 6.10 (d) KOH/urea 5.34 (e) KOH/urea 4.75.

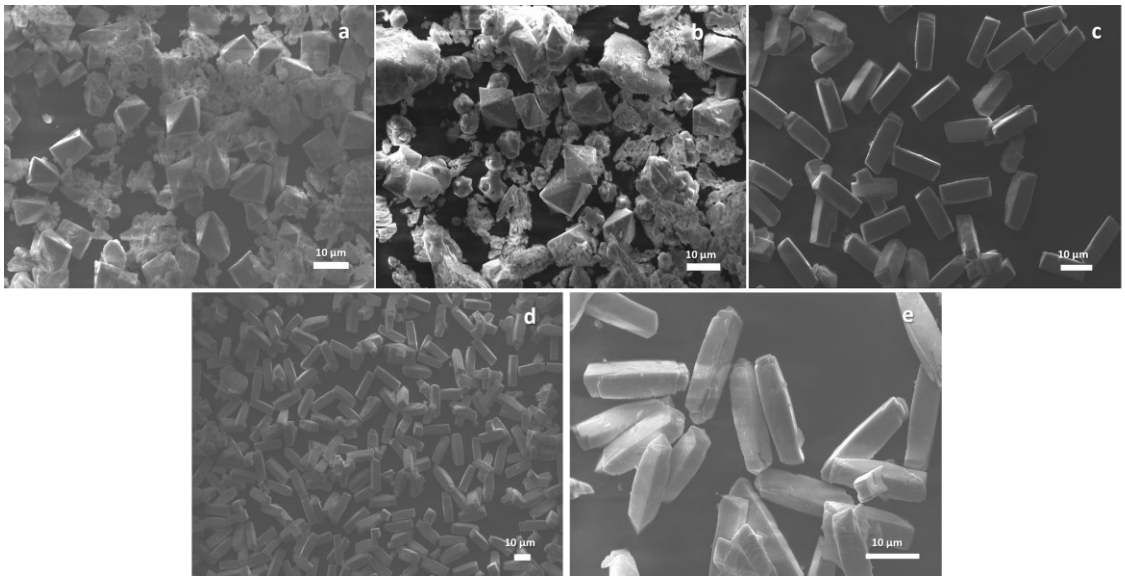

Figure 21. SEM images of the effect of the amount of KOH/urea molar ratio in Series 2: (a) KOH/urea 10.17 (b) KOH/urea 8.72 (c) KOH/urea 7.63 (d) KOH/urea 6.78 (e) KOH/urea 6.10.

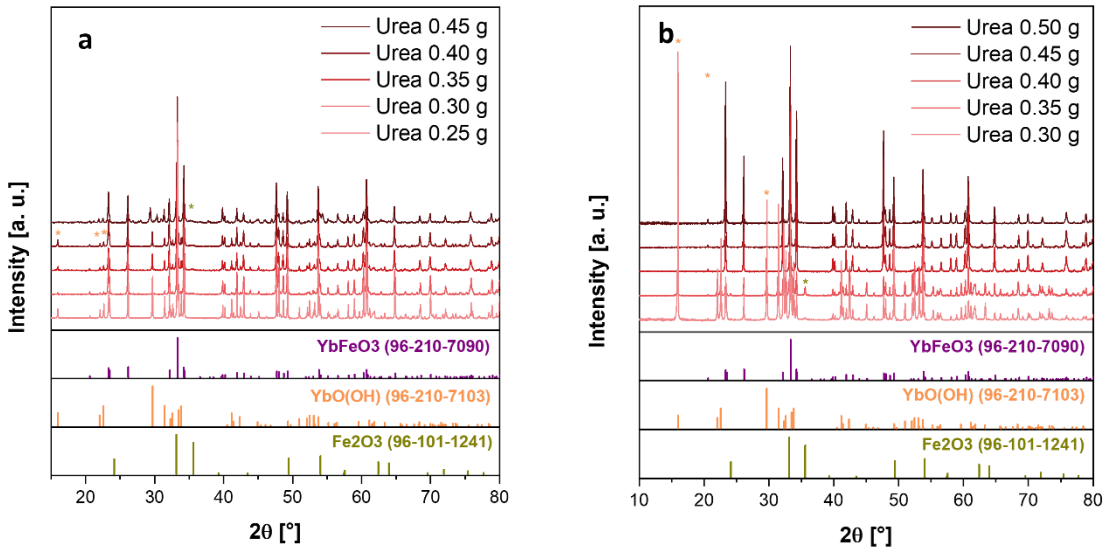

Figure 22. XRD patterns of (a) Serie 1 and (b) Serie 2.

The first observation that was made is that as the amount of urea increased, which means a decreasing KOH/urea molar ratio, the shapes were more elongated, eventually becoming fibrous when the ratio was less than 6. No specific correlation was observed between the formation of secondary phases (Figure 22) and the ratio between the bases. The most interesting results regard the second series, especially for the sample with a KOH/urea molar ratio of 7.63 (Figure 21 (c)) which had an elongated morphology and a pure phase of $YbFeO_3$.

7.5.2 Effect of KOH in Hydrothermal synthesis of $YbFe_{0.95}Co_{0.05}O_3$

In the case of the tests by varying the amount of KOH, first of all it can be seen that the microparticles obtained were all bipyramidal in shape (Figure 23). As no synthesis with a KOH/urea molar ratio below 6 was performed, no fibrous forms of the material were observed. Also in this synthesis, as in the previous tests, there was no correlation between impurities (Figure 24) and molar ratio between the bases. The most interesting result from this series was the last one, from a KOH/urea molar ratio of 18.17 (Figure 23 (d)), which was composed of a pure phase of the perovskite with the morphology of bipyramids.

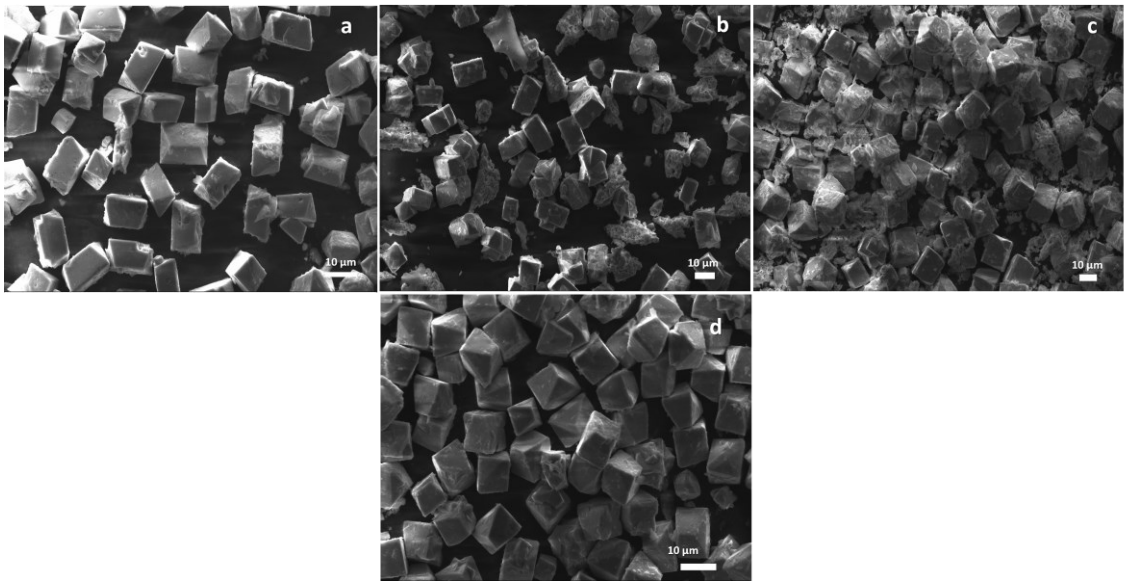

Figure 23. SEM images of the effect of the amount of KOH/urea molar ratio: (a) KOH/urea 7.12 (b) KOH/urea 10.90 (c) KOH/urea 14.53 (d) KOH/urea 18.17.

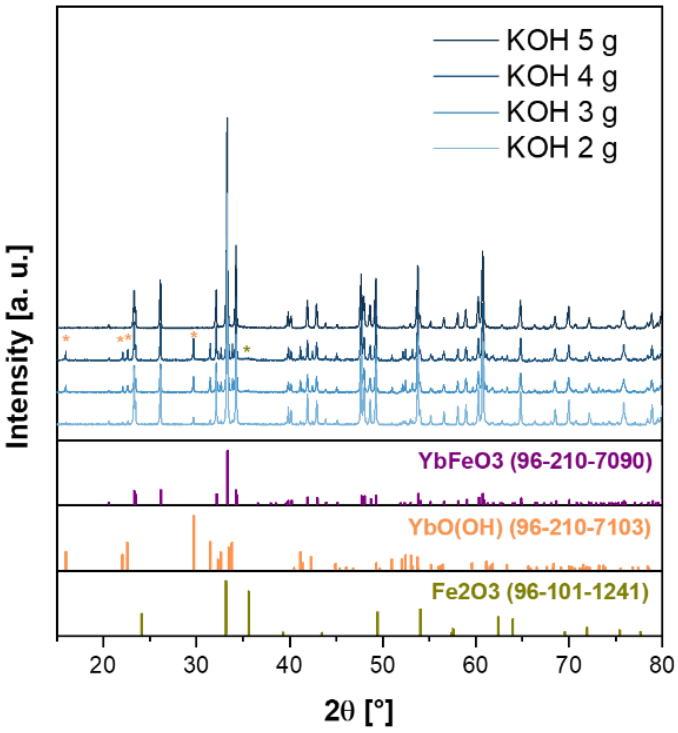

Figure 24. XRD patterns of KOH effect at constant urea.

In order to clarify whether or not the incorporation of the dopant in the perovskite crystal structure of the stoichiometric material was successful, XAS measurements at the Co K-edge (E_{Co} = 7709 eV) were performed. Here is reported and discussed the

XANES spectrum of the stoichiometric elongated microparticles, obtained from a KOH/urea molar ratio of 7.63 (see Section 7.5.1), (Figure 25).

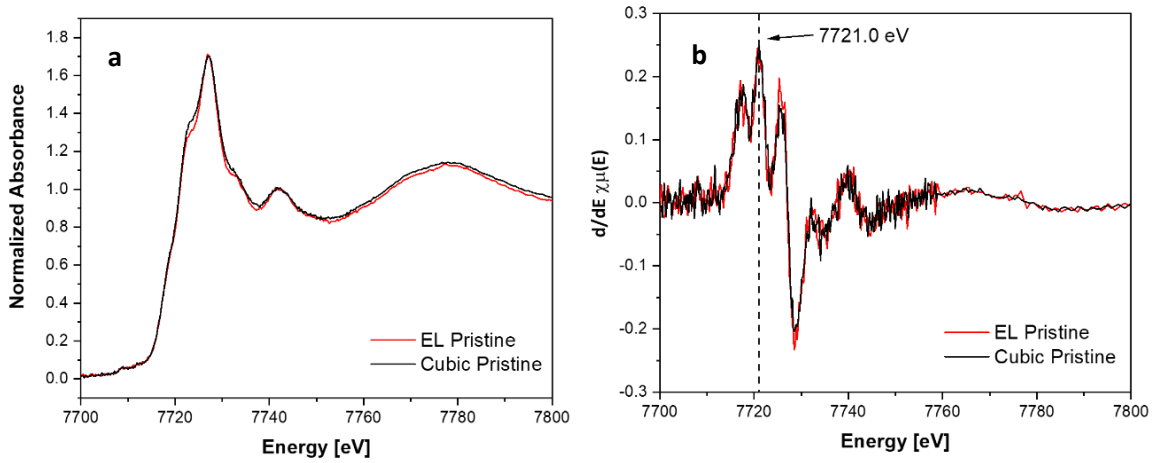

Figure 25. (a) Normalized XANES spectra and (b) first-order derivative of XANES Co K-edge in Co-doped non-stoichiometric $Yb_{0.95}Fe_{0.95}Co_{0.05}O_3$ cubic and stoichiometric elongated tetragons microparticles of $YbFe_{0.95}Co_{0.05}O_3$.

The XANES spectrum of the stoichiometric material was compared with the non-stoichiometric one, already analysed and discussed in the previous subchapter 7.2. In Figure 25 it is clearly visible how the two spectra overlap almost perfectly suggesting that the introduction of A-site deficiency in the material did not affect the state and the environment of the Co in the sample. Also, the first derivatives are superimposable and present the same value of edge energy at 7721.0 eV. Therefore, the same conclusions drawn for the stoichiometric material also apply to the non-stoichiometric one. In conclusion, there is much evidence to assume that Co was not in the octahedral environment typical of the B-site positions of the perovskite as Co^{3+} but rather, it was present as Co^{2+} in its oxide Co(II) form (CoO).

7.6 Exsolution behaviour of anisotropic $YbFeO_3$ microparticles

7.6.1 Investigation of the behaviour of the undoped microparticles to find the best temperature treatment

First of all the exploration of different temperatures for the reduction treatment was carried out on the undoped $YbFeO_3$ to understand how the material behaved in such conditions. The aim of this study was to find the optimal temperature to perform the exsolution of Co from the doped perovskite, while avoiding the formation of secondary phases. This investigation was performed on the $YbFeO_3$ with cubic morphology in the temperature range from 500 to 900 °C with treatment time of 30 minutes, under a reducing atmosphere of hydrogen. It was assumed that the observations made for cuboids could be extended to the other two shapes, as the chemical characteristics of the materials were the same.

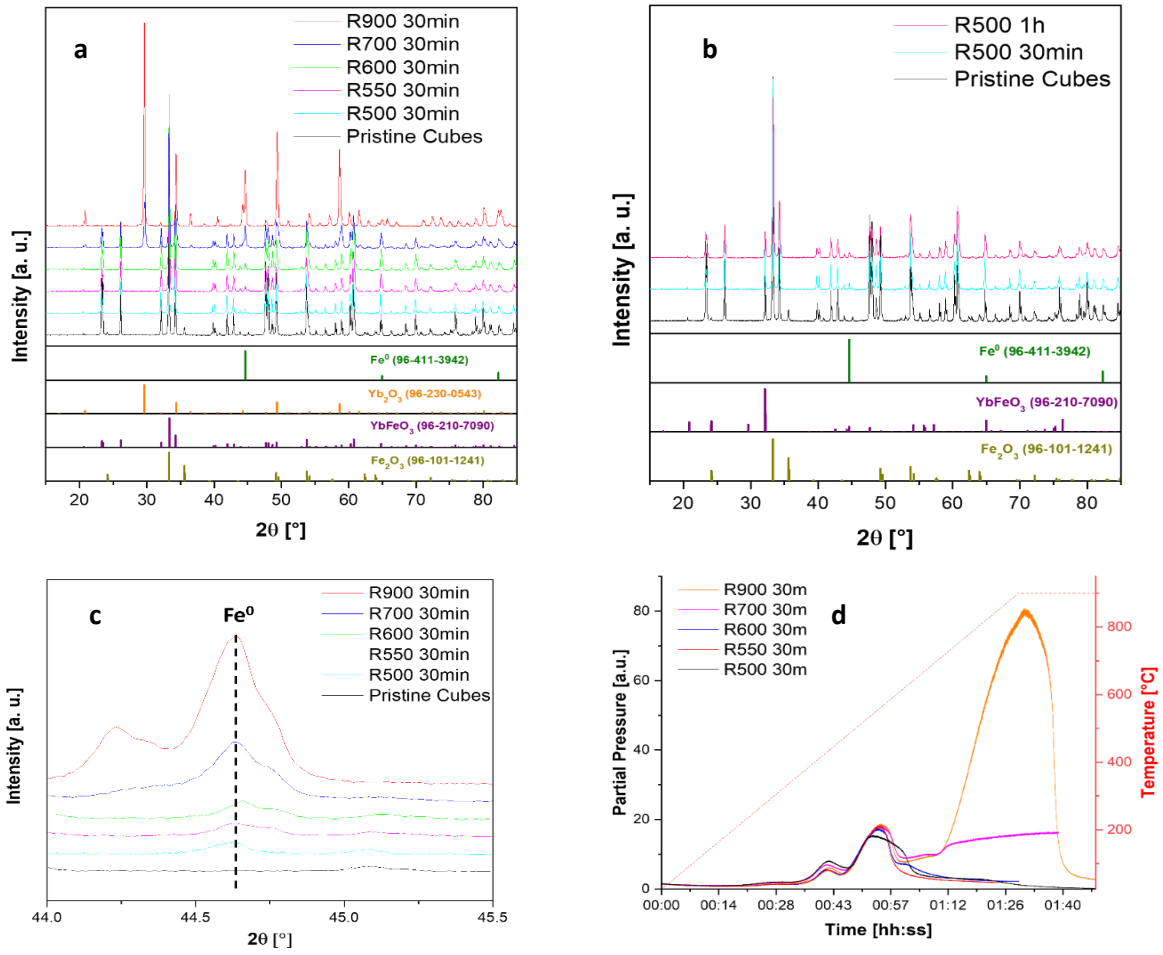

Figure 26. (a) XRD patterns of reduced $YbFeO_3$ at different temperatures for 30 minutes; (b) XRD patterns of reduced $YbFeO_3$ at 550 °C for 30 minutes and 1 hour; (c) increasing intensity of the reflection of metallic α-Fe with increasing temperature; (d) Temperature Programmed Reduction (TPR) of the reduction treatments of $YbFeO_3$.

For a more complete understanding of the reduction events occurring in the materials, SEM, XRD, in situ mass spectrometry (MS) during reduction and XANES measurements were carried on the samples after each treatment. Thanks to the XRD analysis, reported in Figure 26 (a), the evolution of crystalline phases in the materials due to changes in the temperature could be observed. It could be stated that the material remained stable up to 550 °C, as the orthorhombic $YbFeO_3$ phase was preserved. Starting from 600 °C, the more intense and characteristic reflection of cubic Yb_2O_3 (at 30 2θ°) [120] began to appear and became more intense as the temperature increased, eventually completely replacing the perovskite phase following the treatment at 900 °C. The disappearance of the Fe_2O_3 Signal at 34.5 2θ° and the appearance of a new reflection at 44.6 2θ°, attributed to the metallic α-Fe phase [121],

were evident already after the treatment at 500 °C. The variation of the dwelling time was also explored with a one-hour treatment at 500 °C. No notable differences with the 30-minutes treatment were discernible (Figure 26 (b)).

To monitor the reduction process, mass spectrometry (MS) was employed since it provides valuable insights into the material's reduction when subjected to high-temperature treatment with hydrogen. The reduction of Fe^{n+} is directly related to the release of lattice oxygen. Therefore, the evolution of the water signal, shown in Figure 26 (d), was closely tracked because it provides insights into the diffusion and release of oxygen from the host perovskite. Coupling this measurement with the XRD results enabled a comprehensive understanding of the reduction mechanism. In the lower temperature range, between 150 and 500 °C, the water release patterns overlapped, suggesting a consistent behaviour of the materials. The first peak, around 230 °C, represents the desorption of weakly adsorbed water, volatile substances or the OH moieties formed on the oxide surface produced by the hydrothermal synthesis [122]. At 370 °C, the second surface species release event began, followed by a more intense water signal at 480 °C. Zao et. al [123] studied the reduction events of $LaFe_{1-x}Co_xO_3$ observing a first water release peak between 400 °C and 600 °C which was related to the reduction of Fe^{4+} to Fe^{3+} upon the consumption of adsorbed oxygen. The temperature differences of the reduction events between the TPRs reported here and the literature [124] are probably due to the different type of material and the synthesis by which it was obtained. In the case of the material discussed in this work, it could be that it was particularly poorly resistant to high temperatures and therefore easily reducible. This would explain the reduction of iron oxide to metallic iron as observed in the diagrams. A prominent water release signal, characterising the treatment at 900 °C, extends from 700 °C to the plateau. This was associated with the decomposition of the $YbFeO_3$ in the two phases of Yb oxide and Fe^0, as shown in the XRD results. The onset of this event was also visible during the treatment at 700 °C, although the peak was truncated probably due to the temperature not being sufficiently high to fully accomplish the reduction event. The same hypothesis could be advanced regarding the small signal that starts around 600 °C in the equivalent treatment. In the TPR profiles of the three highest temperature treatments, a modest water release was formed in the range between 600 and 700 °C, likely associated with the initial stage of the reduction

of Yb^{3+} to Yb^{2+}, which ultimately led to the complete decomposition of the perovskite. This was confirmed by the XRD patterns, where the coexistence of three crystalline phases ($YbFeO_3$, Yb_2O_3 and Fe^0) characterised the material treated at 600 and 700 °C.

The XANES measurements at the Fe K-edge (E_{Fe} = 7112 eV) are reported in Figure 27 and this data is consistent with the XRD results. The gradual reduction of the material as a result of the increase in the temperature treatment was demonstrated by the shift of the absorption edge towards lower energies and it was a confirmation of the progressive decrease in the oxidation state of the Fe [125]. The shape of the spectrum of the pristine material was in accordance with the literature [126]. The pre-edge peaks, around 7114 eV and 7115 eV were related respectively to the transitions to spin down states due to the Fe-O bonds, and to the spin up states as a consequence of Fe-Fe next neighbour hybridization states [127]. The maximum of the absorption was at 7129 eV and was followed by two shoulders in the higher energy flank. This information suggested the Fe^{3+} being in the octahedral coordination typical of the perovskite B-sites. The gradual change in the shape of the XANES of the various materials reflects the change in the coordination environment of Fe. At 900 °C the shape of the XANES spectrum completely changed and resembled to the one of the Fe foil indicating the reduction to the metallic state [128]. This was related to the complete decomposition of the material which was furthermore corroborated by the XRD results, showing the loss of structural integrity at this temperature. Even at temperatures as low as 500 °C iron was marginally reduced. In fact, temperatures beyond 600 °C revealed exsolution of iron to a larger extent, which could be seen both in the increasing intensity of the Fe^0 reflection in the XRD (Figure 26 (c)) and in the progressive decreasing of the absorption edge in the XANES (Figure 27). This observation was supported by the fact that iron reduction between 500 and 600 °C remained almost unaltered.

SEM images of the samples (Figure 28) were particularly interesting for the high temperature treatments (900 °C and 700 °C) where the effect on the overall structure of the material could be seen. The morphology and the average size distribution of the microparticles remained unchanged, while some spheric nanoparticles started to appear on the surfaces after 700 °C, especially along the edges, and became even more present on the sample upon 900 °C treatment: here the surfaces were more blurred and rougher. This was associated with the phase separation shown in the XRD and the

reduction evidenced in XANES results. The observed decomposition of the perovskite matrix driven from the formation of Yb_2O_3 and metallic Fe as indicated by the merging reflections of the respective phases. This result is quite surprising since the cuboidal morphology was retained even though the perovskite phase completely disappeared from the XRD pattern. With regard to the SEM of the material treated at mild temperatures (Figure 28 (b)-(e)), no nanoparticles were visible on the surfaces which could be due to the low resolution of the instrument and to the fact that usually iron is not easy to exsolve due to its low co-segregation energy [129].

From all these results it could be stated that the optimal temperature range for carrying out exsolution on the Co-doped $YbFeO_3$ was between 500 and 550 °C (mild temperature range) since the reduction of the material already occurred while preserving the perovskite matrix.

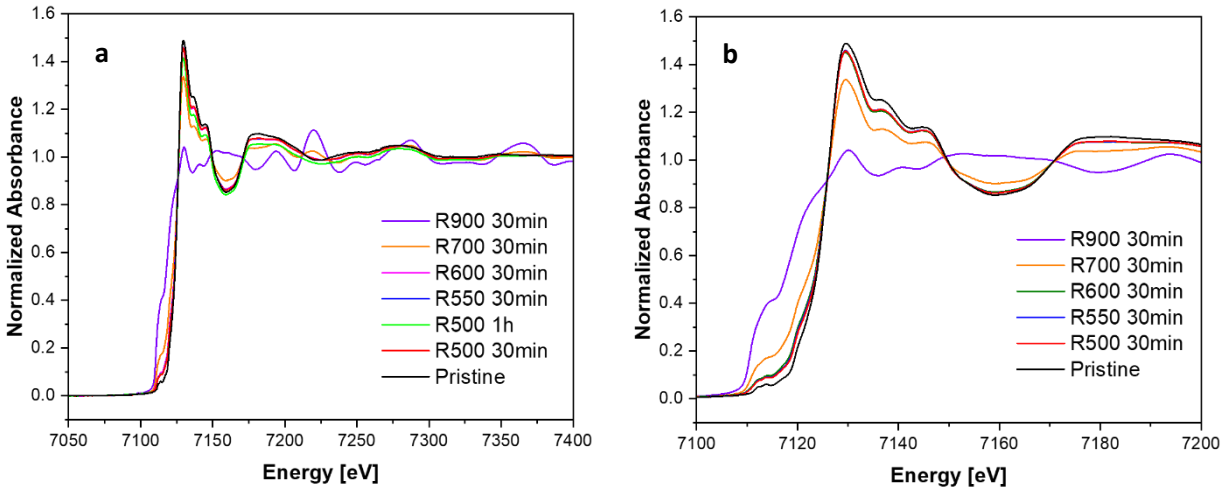

Figure 27. Normalized XANES spectra (a) in the 7050-7400 eV energy range and (b) in the 7100-7200 eV energy range of XANES Co K-edge in Co-doped non-stoichiometric cubic microparticles of $YbFeO_3$ treated under different reduction conditions.

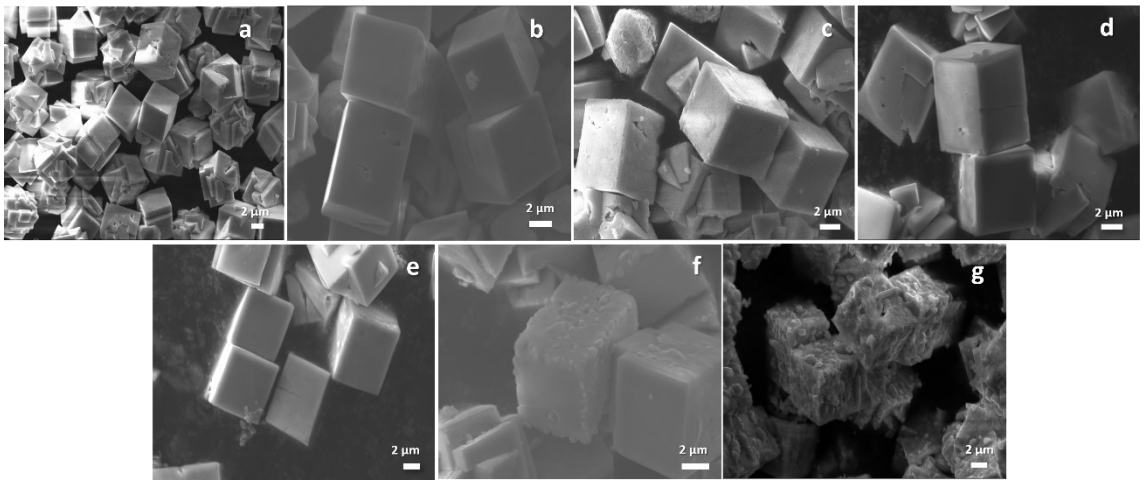

Figure 28. SEM images of: (a) pristine $YbFeO_3$ microparticles and the same sample after reduction treatment (b) at 500 °C for 30 minutes; (c) at 550 °C for 1 hour; (d) at 550 °C for 30 minutes; (e) at 600 °C for 30 minutes; (f) at 700 °C for 30 minutes and (g) 900 °C for 30 minutes.

7.7 Exsolution of Co-doped $YbFeO_3$

Having established that the best temperature to preserve the perovskite structure during heat treatment of Yb microparticles was between 500 and 550 °C, the exsolution of Co from the doped material was performed at this temperature. From the various synthesised samples, those with the lowest degree of secondary phases and the best quality in terms of shape and surface were selected. Mass spectrometry, XRD, XANES and SEM analyses were used to study and follow the exsolution process. The results are reported and discussed below by discriminating on the morphology of the microparticles.

7.7.1 Cuboids

The cuboids were treated for 30 minutes at 500 °C and 550 °C. As phase separation was observed at temperature above 600 °C, treatments with longer dwell times at low temperatures were also explored: 1 hour and 5 hours at 500 °C. The XRD, reported in Figure 29 (a), showed that the perovskite phase was completely retained up to 1 hour treatment while, after 5 hours, the phase separation began with the appearance of the characteristic reflection of Yb_2O_3 at 30 2θ°. A slight shift of the reflections of the reduced diffractogram toward smaller angles was notable, as a consequence of the exsolution

process leading to a shrinkage of the cell. In addition, the presence of a new reflection at 44.8 2θ° was noted in the diffractograms of the material after reduction. This signal was related to a Co/Fe alloy and increased in intensity with increasing treatment time and it was a confirmation of metal reduction [130]. No particular differences could be seen between the 500 and 550 °C treatments.

The water release signal is showed in the TPR plots in Figure 29 (c) and (d). The perfect overlapping of the plots suggested that the oxygen released from the material was consistent, that means that the reduction events that occurred in the material were always the same in every treatment. The first water release signal, around 200 °C, was due to desorption of surface species, like residual water or carbonates. This peak is followed by another shoulder at 370 °C circa, which was not visible in the case of undoped material. This suggested that doping enhance oxygen diffusion. The most prominent water release signal starts at 430 °C. This hydrogen consumption events are close in temperature to those observed for the undoped $YbFeO_3$ microparticles and could therefore be related to the progressive reduction of Fe to lower oxidation states, as demonstrated by the XRD reflection. Roseno et al. report TPRs of $LaCoO_3$, $LaFeO_3$ and $LaCo_{0.5}Fe_{0.5}O_3$ [124] and Brackmann et al. [131] studied the reduction of $LaCoO_3$, both suggesting that the reduction of Co^{3+} to Co^{2+} happens in the range between 300 and 500 °C, followed by the one that leads to metallic Co between 500 and 600 °C. This allowed us to assume that the shoulder to the right of the most intense signal, at about one hour of treatment and at 500 °C, was due to the complete reduction of Co, in accordance with the diffractograms.

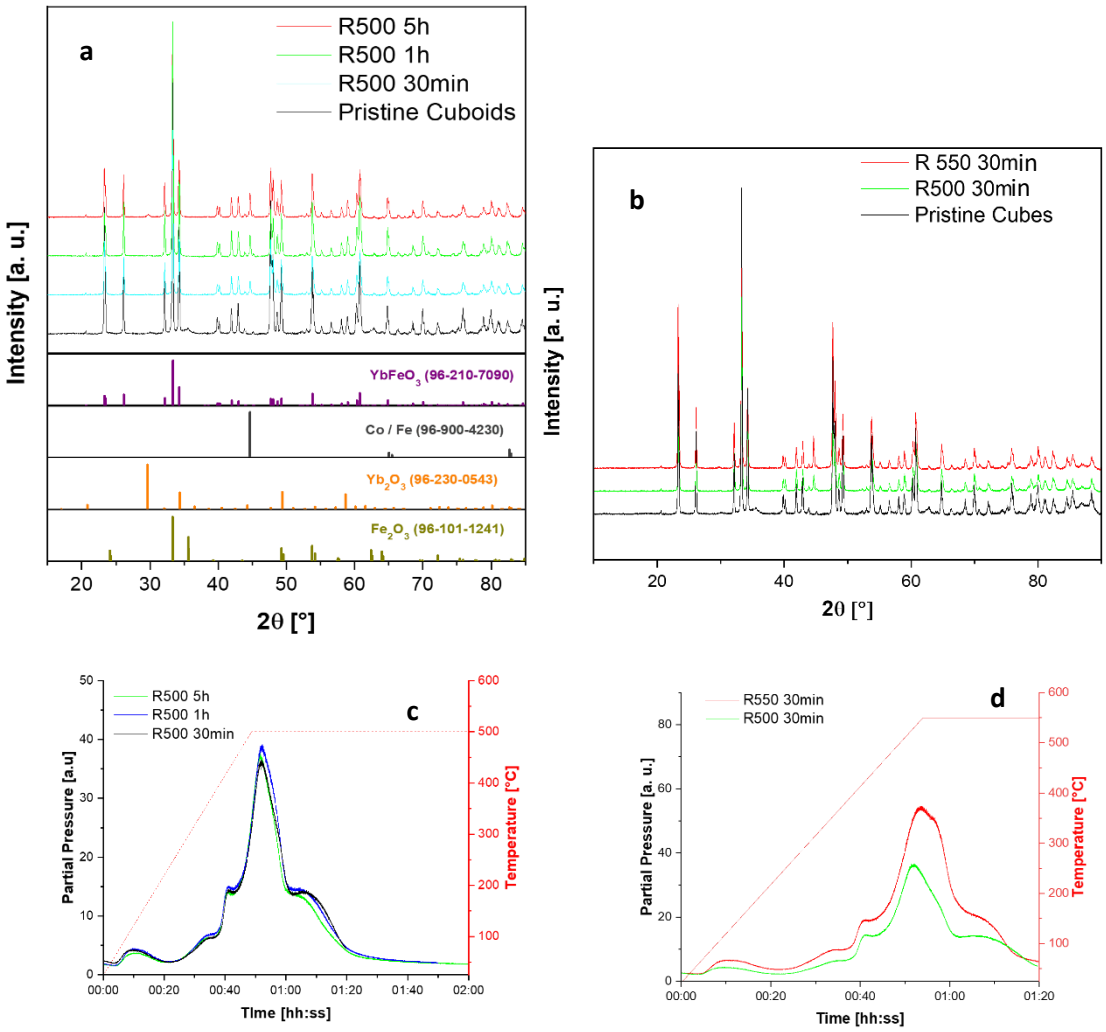

Figure 29. XRD pattern of non-stoichiometric Co-doped cuboids microparticles (a) after 500 °C reduction at different treatment times and (b) after 500 and 550 °C reduction at 30 minutes; TPRs of the exsolution treatments (d) at 500 °C for different dwelling times and (e) at 500 and 550 °C for 30 minutes.

7.7.2 Elongated microparticles

The elongated tetragons were treated at 500 and 550 °C for 30 minutes. From the XRD results (Figure 30 (a)) it could be said that the material was preserved after both treatments since no phase separation occurred. The pristine material presented a lower amount of both Fe_2O_3 and YbO(OH) impurities and the first one disappeared after the

exsolution treatment. The reflection at 44.8 2θ°, ascribed to the Co/Fe alloy, appeared already upon the 500 °C processing, meaning that the reduction process occurred.

The TPR of the two treatments (Figure 30 (b)) showed a similar behaviour to the cuboids, with a big water release peak that starts at 400 °C, preceded by a shoulder at slightly lower temperatures which could be related to the reduction of Fe, and followed by another shoulder after 500 °C due to Co reduction.

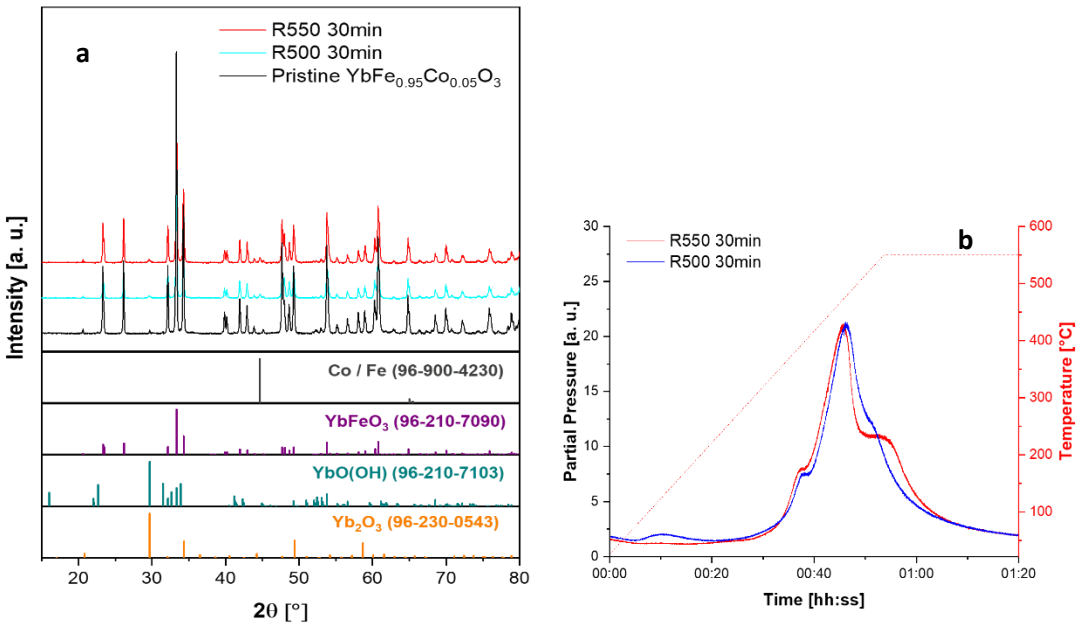

Figure 30. (a) XRD patterns of stoichiometric elongated $YbFe_{0.95}Co_{0.05}O_3$ microparticles after 500 and 550 °C reduction treatments; (b) TPR plots of the exsolution of stoichiometric $YbFe_{0.95}Co_{0.05}O_3$ elongated microparticles at 500 and 550 °C.

7.7.3 Bipyramids

As for the previous sample, the bipyramids were kept at 500 °C and 550 °C under reducing atmosphere for 30 minutes to study the exsolution behaviour. From the diffractograms (Figure 31 (a)) is visible how the crystalline phase of the material changed after the treatment. In this case, the microparticles seemed to be stable up to 500 °C because, after the higher temperature treatment, a modest reflection of Yb_2O_3 started to appear. Also in this case, as observed for the other two morphologies, the Co/Fe signal showed up at 44.8 2θ°. The mass spectrometry analysis (Figure 31 (b)) showed an intense water signal that starts at 440 °C with a left shoulder around 400 °C probably

related to Fe reduction. The right shoulder after 500 °C is not visible in the TPR of the lower temperature treatment, while is present in the one at 550 °C.

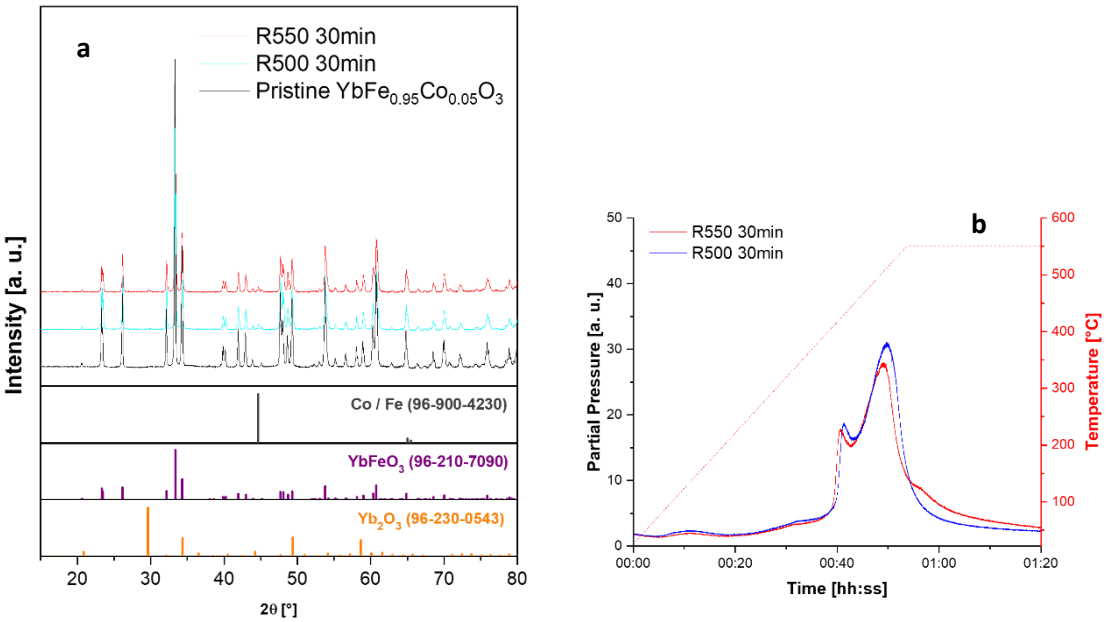

Figure 31. (a) XRD patterns of stoichiometric bipyramidal $YbFe_{0.95}Co_{0.05}O_3$ microparticles after 500 and 550 °C reduction treatments; (b) TPR plots of the exsolution of stoichiometric $YbFe_{0.95}Co_{0.05}O_3$ bipyramidal microparticles at 500 and 550 °C.

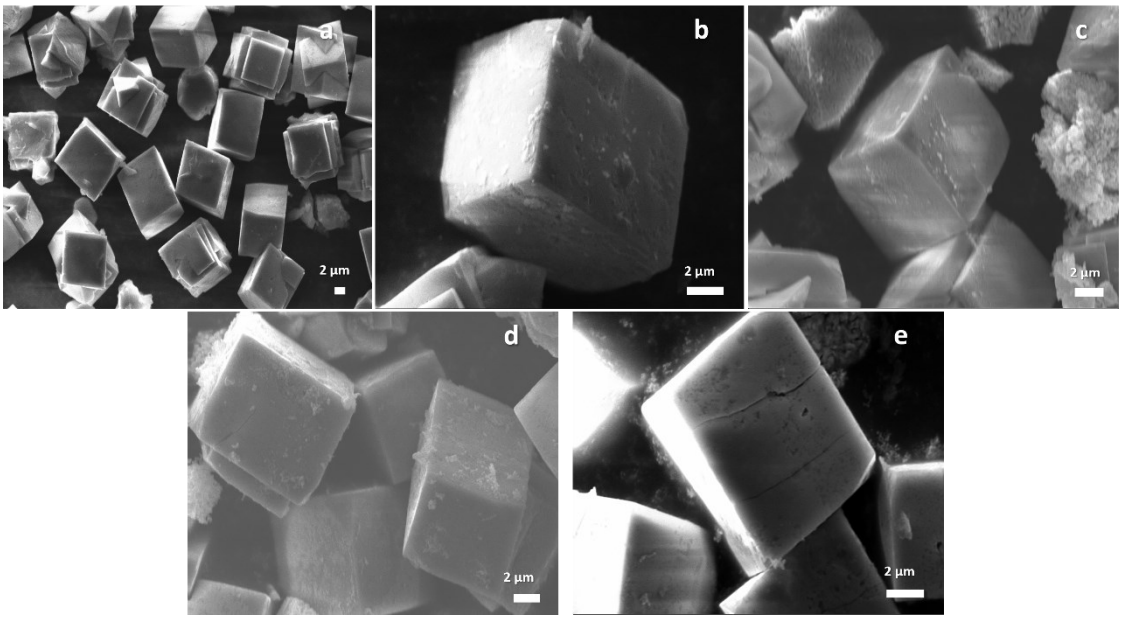

Figure 32. SEM images of (a) cubic pristine $Yb_{0.95}Fe_{0.95}Co_{0.05}O_3$ microparticles and the same sample after the exsolution treatments at (b) 500 °C for 30 minutes; (c) 500 °C for 1 hour; (d) 500 °C for 5 hours; (e) 550 °C for 30 minutes.

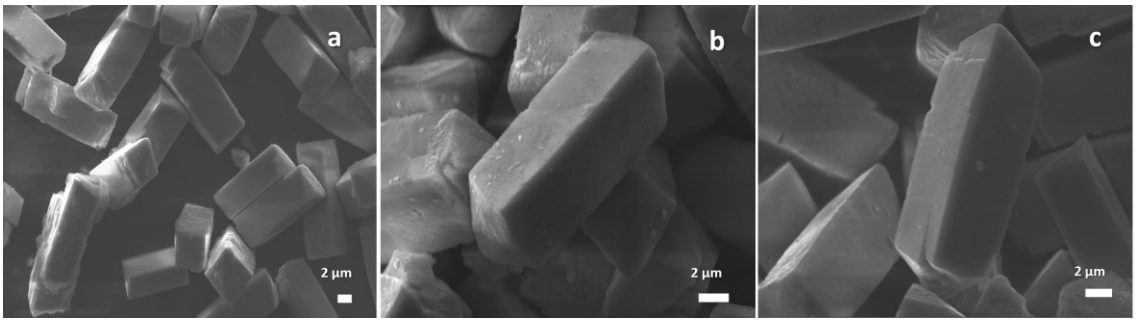

Figure 33. SEM images of (a) elongated pristine $YbFe_{0.95}Co_{0.05}O_3$ microparticles and the same sample after the exsolution treatments at (b) 500 °C for 30 minutes and (c) 550 °C for 30 minutes.

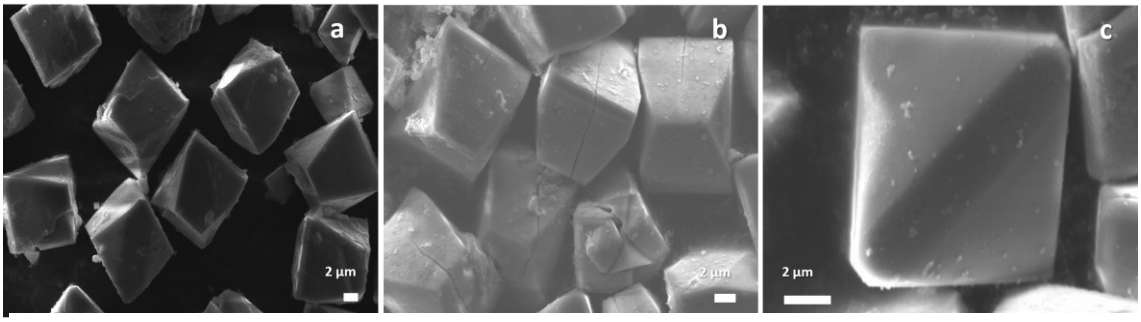

Figure 34. SEM images of (a) bipyramidal pristine $YbFe_{0.95}Co_{0.05}O_3$ microparticles and the same sample after the exsolution treatments at (b) 500 °C for 30 minutes and (c) 550 °C for 30 minutes.

The SEM images of the samples (Figures 32, 33 and 34) present all the same characteristics, so they are described and discussed in a general way. First of all, no exsolved nanoparticles were visible on the surfaces of the microparticles, due to the low resolution of the instrument used. Exsolved nanoparticles are usually between 10 and 50 nm in size [80,96], and rarely exceed hundreds of nm [132]. The highest magnification of the used microscope did not exceed a resolution of 2 µm thus unable to resolve the expected nanoparticle size. The reduced microparticles exhibited no significant differences compared to the pristine material, except for the presence of some agglomerates, which became more conspicuous with temperature increase. This was also observed in the undoped $YbFeO_3$, likely attributed to the temperature-induced agglomeration and crystallisation of some materials. Regarding bipyramids, some cracks were visible already after the 500 °C treatment. This suggests that this sample was more

delicate and temperature sensitive as also shown by the phase separation in the XRD, though the images did not confirm particle formation at the surface after exsolution. Wang et al. investigated the effect on the parent host oxide after exsolution revealing a surface reconstruction concerning a highly Fe-deficient near-surface layer, and a partially polycrystalline surface [133]. A change in surface chemistry and structure generally characterises the exsolution [84] and could therefore also be extended to this work, even though there was no visible evidence from SEM images. Some studies investigate the exsolution of CoFe alloy nanoparticles on various perovskites [77,78,134] showing that, after reduction, the exsolution of CoFe alloy nanoparticles occurs leading to a perovskite substrate with cation vacances. It can be assumed that the formation of oxygen vacances due to the release of oxygen was accompanied by the formation of metallic Co and Fe, as shown in the XRDs (and confirmed by XANES).

It is also worth discussing the difference that can be seen in the reduction trends recorded for the various morphologies (Figure 35). The release of water during the thermal treatment is directly related to the oxygen release from the perovskite host and thus to the reduction of the metals. Firstly, the diverse oxygen diffusion paths that oxygen could take within the lattice and on the surfaces of the microparticles varies with their shapes, thus different signal will be generated. The morphology of the microparticles seemed to exert a discrete influence on the reduction kinetics of the material. Indeed, it could be seen that the cuboids exhibited a delayed reduction. A hypothesis could be formulated based on the SEM image of the undoped cuboid microparticles post-reduction at 700 °C (Figure 28 (f)), suggesting that the reduction might originate from the edges. Taking this observation into consideration, it became rational to assume that elongated and bipyramidal microparticles, characterised by more edges, experienced a faster reduction. Furthermore, the surface terminations, composition, surface area and defect configurations of perovskite oxides are very important for exsolution [122]. The different morphologies were characterised by various orientations and terminations and tush different metal-to-oxygen ratio on the surface. This led to different oxygen release and, in turn, strongly influenced the segregation energy of the nanoparticles [83].

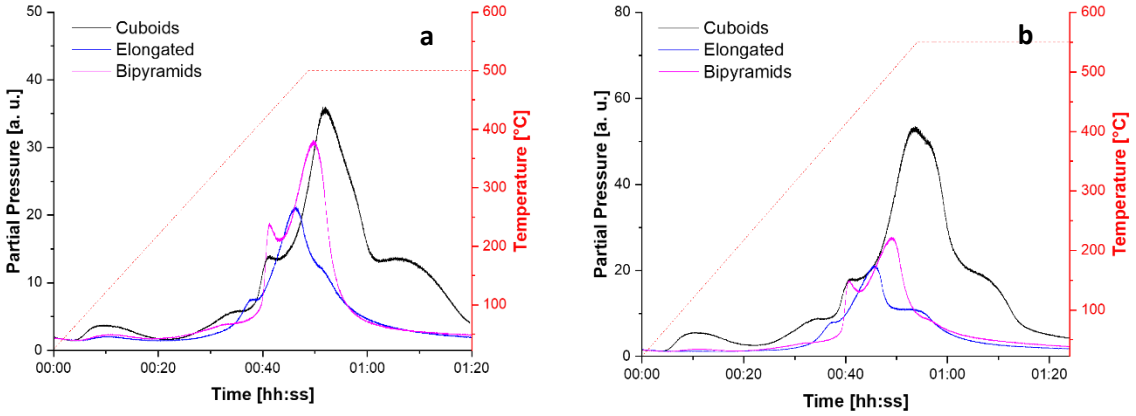

Figure 35. Comparison of the TPR of the exsolution treatments for all the three morphologies at (a) 500 °C and (b) 550 °C for 30 minutes.

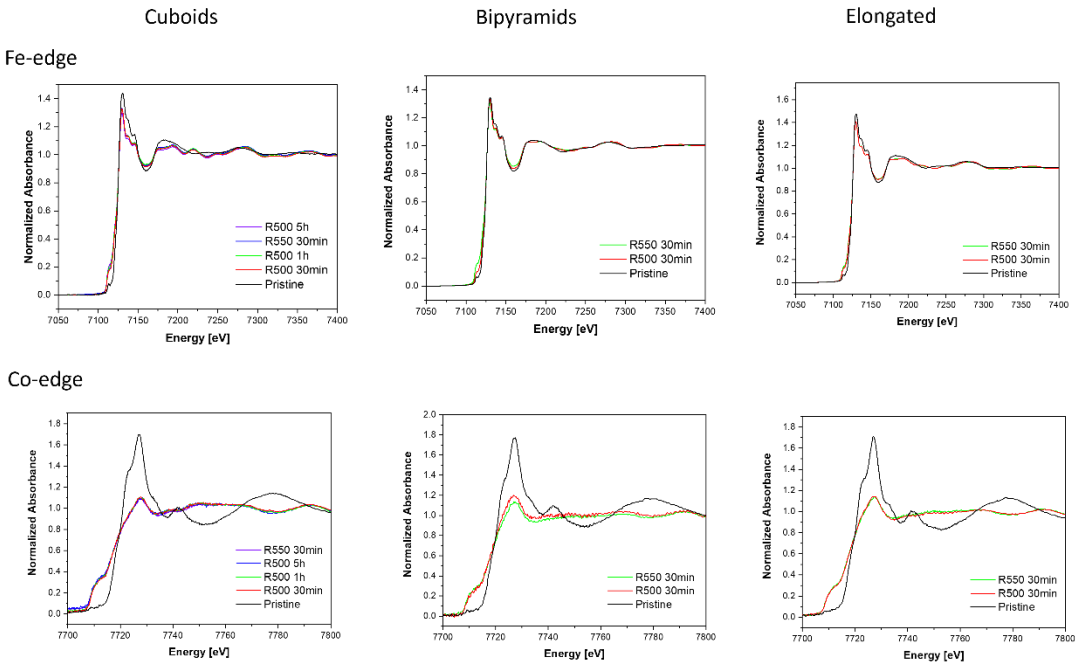

Figure 36. Normalized XANES spectra of XANES Co K-edge and Fe K-edge in Co-doped non-stoichiometric cuboids and stoichiometric elongated and bipyramidal microparticles of $YbFeO_3$ treated under different reduction conditions.

The XANES of Fe–K (E_{Fe} = 7112 eV) and Co–K (E_{Co} = 7709 eV) edges in a series of Fe- and Co-containing samples characterized by different morphologies were measured in transmission mode and florescence mode, respectively, and are reported in Figure 36. The Co-doped microparticles were treated at 500 °C and 550 °C to make the exsolution happen. Within the mild temperature range used, iron was reduced from the doped material as demonstrated by the decreasing of the white line as well as the shift to lower energies as was observed in the undoped material. No substantial changes were observed for the increase of temperature, as evidenced by the XANES spectra that result superimposable for the 500 and 550 °C 30 minutes treatment across all the samples. However, the increase of the reduction time (from 30 minutes, to 1 hour and finally to 5 hours) led to an enhanced exsolution, clearly visible from the gradual decrease of the absorption Fe-edge peak in the XANES spectra of the cuboids (Figure 36) ascribed to the decrease of the oxidation state and to the variation of the chemical environment of the absorber. The main difference regards the 500 °C treatment at 5 hours. This was congruent with the XRD results, with the progressive increase intensity of the Fe^0 reflex and the emergence of the secondary phase of Yb_2O_3, observed for the longer time treatment. As regards the XANES measured at Fe K-edge (7112 eV), the sharpness of the peak had vanished compared to the undoped sample. This was due to the presence of Co in the samples. The dopant, which has a negative reduction potential, was introduced in the perovskite matrix to favour the reduction of Fe, which has a slight positive ΔG (for $Fe^{2+} \rightarrow Fe^0$ reduction) [25,80]. The resulting mixed cation system was more easily reducible than the undoped counterpart and this led to an attenuation of the XANES absorption edge.

The shape of the XANES spectra for Co-edge was the same for all morphologies and exsolution treatments. Comparing these trends with the references of metallic Co found in the literature [115], it was assumed that the metal was completely reduced to its fundamental state after each heat treatment at mild temperature.

8 Conclusions and Outlooks

This thesis work provided interesting experimental results concerning the hydrothermal synthesis of crystalline microstructures of $YbFeO_3$, pure and doped with Co, with controlled morphology simply by varying the molar ratio of the bases used for the reaction (KOH and urea). The obtained powders were composed of microparticles in the micrometre size region (with edges sizes varying from 7 to 17 μm depending on the shape). The study at high temperature in a reducing atmosphere shed light on the exsolution behaviour of the synthetised material and on the relationship between microparticle shape and reduction.

In the first part of the work reported in this thesis, the hydrothermal syntheses of $YbFeO_3$ microparticles with three different morphologies (cuboids, elongated tetragons and bipyramids) were successfully performed. The obtained shapes depended on the concentration ratio between the bases used for the reaction: KOH and urea. This was followed by the hydrothermal synthesis of $YbFeO_3$ microparticles doped at 5% at Co, maintaining the same protocol followed for the synthesis of pure ferrite. Since microparticles were synthesised in order to study their behaviour under exsolution conditions, the first doped material to be synthesised was non-stoichiometric, specifically with A-site deficiency and with formula $Yb_{0.95}Fe_{0.95}Co_{0.05}O_3$ (although just nominally, since the A-site deficiency was not demonstrated). SEM images showed that the obtained microparticles were characterised by surface imperfections and multiple facets growth of the particles. In addition to the main orthorhombic phase of $YbFeO_3$, a secondary phase of iron oxide was also present in the sample. Thus, hydrothermal synthesis at higher temperatures was explored to improve the phase purity. It was seen that temperature had no positive effect on either particle morphology or purity, and at high temperatures the bipyramidal morphology was favoured.

In order to avoid the formation of the secondary phase of iron oxide in the doped particles, an attempt was made to synthesise stoichiometric microparticles (more stable than non-stoichiometric) in which no excess iron was present in the reaction environment. The synthesis of stoichiometric microparticles with formula $YbFe_{0.95}Co_{0.05}O_3$ was then conducted, but without obtaining an improvement of the results. An attempt was therefore made to optimise the synthesis of the doped material

by varying the KOH to urea molar ratio. Two series were prepared in which the amount of urea was varied while keeping the amount of KOH constant. This study showed that, as the amount of urea increased, the particles grew more and more elongated until they became fibrous. The molar ratio of 7.63 led to the interesting result of elongated morphology and pure phase of $YbFeO_3$. Exploration of the effect of KOH was carried out in a series of syntheses at constant urea concentration. In this case, the best result was for a KOH/urea molar ratio of 18.17, which resulted in pure bipyramidal particles. The sample of A-site-deficient cuboids was analysed by XAS technique. An important result was obtained, suggesting the presence of Co^{2+} oxide and, that the dopant was not fully incorporated into the B-sites of the perovskite matrix. From the performed analyses (XRD, XANES and SEM), it was reasonable to assume that stoichiometric ytterbium ferrite would therefore appear to be the most stable and preferred form from this hydrothermal synthesis.

In the second part of this thesis, the as prepared ytterbium ferrite was treated at high temperatures and in a reducing atmosphere to study the exsolution of metals from the host perovskite. The pure material with cuboidal morphology was treated first. Various temperatures in the range of 500 to 900 °C were explored as a function of time. At temperatures above 600 °C, phase separation of the perovskite began, while at 900 °C, the complete decomposition of the crystal structure occurred. Thanks to this study, it was possible to determine that the optimum temperature for reduction treatment was between 500 and 550 °C, for 30 minutes (mild conditions). In this interval, the $YbFeO_3$ phase was preserved. The three doped microparticle morphologies were then treated. All samples were analysed by SEM, XRD, MS and XAS (XANES). From these analyses, it could be seen that the Fe and Co metals in the perovskite matrix were reduced at temperatures as low as 500 °C, and that the reduction extent increased with increasing temperature and treatment time. It was also observed that the reduction appeared to start at the edges of the microparticles. The most interesting result was that the reduction kinetics of the material was influenced by the morphology of the microparticles. Cuboids showed a delayed reduction compared to elongated microparticles and bipyramids, the latter also showing cracks on the surfaces already after treatment at 550 °C. The resulting reduction trend may be related to the

preferential reduction along the edges, which were more pronounced in the case of elongated and bipyramidal particles than in cuboids.

In conclusion the findings of this thesis have shed light on the hydrothermal synthesis of rare earth ferrites and the exsolution behaviour of Co-doped $YbFeO_3$ microparticles. Looking ahead, it is clear that there are many possibilities for future exploration and development in this field. While this research has provided valuable insights, there is still room for further investigation in this area. To achieve a complete understanding of this topic, it is essential to undertake further research focusing on the structure of the material and its fine composition before and after the reduction treatment. To address this, more in-depth analyses are required. High-resolution SEM would make it possible to observe the surfaces more closely and investigate their changes; Energy Dispersive X-ray Spectroscopy (EDX) could be used to determine the exact composition of the samples, and X-ray Photoelectron Spectroscopy (XPS) to probe the chemical environment on the surfaces. The practical applications of this work are noteworthy, particularly in the technology of sensors, as absorbers in solar cells and in catalysis especially as photocatalysis and electrocatalysis. Based on previous studies in the literature, the obtained material could be a good cathode candidate for intermediate-temperature solid oxide fuel cells [112]. Therefore, studies on the catalytic activity of exsolved microparticles could lead to new and exciting developments.

9 BIBLIOGRAPHY

1. Fechete, I., Wang, Y., and Védrine, J.C. (2012) The past, present and future of heterogeneous catalysis. *Catal Today*, **189** (1), 2–27.

2. Derouane, E.G. (2001) Catalysis in the 21st century, Lessons from the Past, Challenges for the Future. *Cattech*, **5**, 214–225.

3. Chen, D., Chen, C., Baiyee, Z.M., Shao, Z., and Ciucci, F. (2015) Nonstoichiometric Oxides as Low-Cost and Highly-Efficient Oxygen Reduction/Evolution Catalysts for Low-Temperature Electrochemical Devices. *Chem Rev*, **115** (18), 9869–9921.

4. Royer, S., Duprez, D., Can, F., Courtois, X., Batiot-Dupeyrat, C., Laassiri, S., and Alamdari, H. (2014) Perovskites as substitutes of noble metals for heterogeneous catalysis: Dream or reality. *Chem Rev*, **114** (20), 10292–10368.

5. Zhu, X., Li, K., Neal, L., and Li, F. (2018) Perovskites as Geo-inspired Oxygen Storage Materials for Chemical Looping and Three-Way Catalysis: A Perspective. *ACS Catal*, **8** (9), 8213–8236.

6. Tilley, R.J.D. (2004) *Understanding solids : the science of materials*, J. Wiley & Sons Ltd, Southern Gate, Chichester, West Sussex, England.

7. Shaikh, S.F., Ubaidullah, M., Mane, R.S., and Al-Enizi, A.M. (2020) Types, Synthesis methods and applications of ferrites, in *Spinel Ferrite Nanostructures for Energy Storage Devices*, Elsevier Science Publishing Co Inc, Verlag, pp. 51–82.

8. Ruh, T., Berkovec, D., Schrenk, F., and Rameshan, C. (2023) Exsolution on perovskite oxides: morphology and anchorage of nanoparticles. *Chemical Communications*, **59** (27), 3948–3956.

9. Cai, L., Bian, F., Chen, H., Guo, J., Wang, Y., and Zhao, Y. (2021) Anisotropic Microparticles from Microfluidics. *Chem*, **7** (1), 93–136.

10. Bae, J., Shin, D., Jeong, H., Choe, C., Choi, Y., Han, J.W., and Lee, H. (2021) Facet-Dependent Mn Doping on Shaped Co_3O_4 Crystals for Catalytic Oxidation. *ACS Catal*, **11** (17), 11066–11074.

11. Walton, R.I. (2020) Perovskite Oxides Prepared by Hydrothermal and Solvothermal Synthesis: A Review of Crystallisation, Chemistry, and Compositions. *Chemistry*, **26** (42), 9041–9069.

12. Li, C., Yang, J., Yang, P., Lian, H., and Lin, J. (2008) Hydrothermal Synthesis of Lanthanide Fluorides LnF_3 (Ln = La to Lu) Nano-/Microcrystals with Multiform Structures and Morphologies. *Chemistry of Materials*, **20** (13), 4317–4326.

13. Einarsrud, M.-A., and Grande, T. (2014) 1D oxide nanostructures from chemical solutions. *Chem. Soc. Rev.*, **43** (7), 2187–2199.

14. Kim, K.J., Han, H., Defferriere, T., Yoon, D., Na, S., Kim, S.J., Dayaghi, A.M., Son, J., Oh, T.S., Jang, H.M., and Choi, G.M. (2019) Facet-Dependent in Situ Growth of Nanoparticles in Epitaxial Thin Films: The Role of Interfacial Energy. *J Am Chem Soc*, **141** (18), 7509–7517.

15. Teoh, W.Y., Urakawa, A., Ng, Y.H., and Sit, P. (2021) *Heterogeneous Catalysts: Advanced Design, Characterization and Applications*, John Wiley & Sons, Inc., Hoboken, New Jersey, United States.

16. Zhang, S., Fan, Q., Xia, R., and Meyer, T.J. (2020) CO2 Reduction: From Homogeneous to Heterogeneous Electrocatalysis. *Acc Chem Res*, **53** (1), 255–264.

17. Wang, S., Lu, A., and Zhong, C.-J. (2021) Hydrogen production from water electrolysis: role of catalysts. *Nano Converg*, **8** (1), 4.

18. Chen, X., Li, Y., Pan, X., Cortie, D., Huang, X., and Yi, Z. (2016) Photocatalytic oxidation of methane over silver decorated zinc oxide nanocatalysts. *Nat Commun*, **7** (1), 12273.

19. Friend, C.M., and Xu, B. (2017) Heterogeneous catalysis: A central science for a sustainable future. *Acc Chem Res*, **50** (3), 517–521.

20. Ponikvar, Ž., Likozar, B., and Gyergyek, S. (2022) Electrification of Catalytic Ammonia Production and Decomposition Reactions: From Resistance, Induction, and Dielectric Reactor Heating to Electrolysis. *ACS Appl Energy Mater*, **5** (5), 5457–5472.

21. Mekuye, B., and Abera, B. (2023) Nanomaterials: An overview of synthesis, classification, characterization, and applications. *Nano Select*, **4** (8), 486–501.

22. Abid, N., Khan, A.M., Shujait, S., Chaudhary, K., Ikram, M., Imran, M., Haider, J., Khan, M., Khan, Q., and Maqbool, M. (2022) Synthesis of nanomaterials using various top-down and bottom-up approaches, influencing factors, advantages, and disadvantages: A review. *Adv Colloid Interface Sci*, **300**, 102597.

23. van Deelen, T.W., Hernández Mejía, C., and de Jong, K.P. (2019) Control of metal-support interactions in heterogeneous catalysts to enhance activity and selectivity. *Nat Catal*, **2** (11), 955–970.

24. Munnik, P., De Jongh, P.E., and De Jong, K.P. (2015) Recent Developments in the Synthesis of Supported Catalysts. *Chem Rev*, **115** (14), 6687–6718.

25. Kousi, K., Tang, C., Metcalfe, I.S., and Neagu, D. (2021) Emergence and Future of Exsolved Materials. *Small*, **17** (21), 2006479.

26. Kim, J.H., Kim, J.K., Liu, J., Curcio, A., Jang, J.S., Kim, I.D., Ciucci, F., and Jung, W.C. (2021) Nanoparticle Ex-solution for Supported Catalysts: Materials Design, Mechanism and Future Perspectives. *ACS Nano*, **15** (1), 81–110.

27. Huang, K., Yuan, L., and Feng, S. (2015) Crystal facet tailoring arts in perovskite oxides. *Inorg Chem Front*, **2** (11), 965–981.

28. Assirey, E.A.R. (2019) Perovskite synthesis, properties and their related biochemical and industrial application. *Saudi Pharmaceutical Journal*, **27** (6), 817–829.

29. Cheng, Z., and Lin, J. (2010) Layered organic-inorganic hybrid perovskites: Structure, optical properties, film preparation, patterning and templating engineering. *CrystEngComm*, **12** (10), 2646–2662.

30. Filip, M.R., and Giustino, F. (2018) The geometric blueprint of perovskites. *Proc Natl Acad Sci U S A*, **115** (21), 5397–5402.

31. Knritle, E., and Jeanloz, R. (1987) Synthesis and Equation of State of (Mg,Fe) SiO_3 Perovskite to Over 100 Gigapascals. *Science*, **235** (4789), 668–670.

32. Li, C., Lu, X., Ding, W., Feng, L., Gao, Y., and Guo, Z. (2008) Formability of ABX_3 (X = F, Cl, Br, I) halide perovskites. *Acta Crystallogr B*, **64** (6), 702–707.

33. Moure, C., and Peña, O. (2015) Recent advances in perovskites: Processing and properties. *Prog in Solid State Chem*, **43** (4), 123–148.

34. Nitadori, T., Ichiki, T., and Misono, M. (1988) Catalytic Properties of Perovskite-Type Mixed Oxides (ABO_3) Consisting of Rare Earth and 3d Transition Metals. The Roles of the A- and B-Site Ions. *Bull Chem Soc Jpn* , **61**, 621–626.

35. Zhu, H., Zhang, P., and Dai, S. (2015) Recent Advances of Lanthanum-Based Perovskite Oxides for Catalysis. *ACS Catal*, **5** (11), 6370–6385.

36. Tilley, R.J.D. (2008) *Defects in solids*, John Wiley & Sons, Inc. , Hoboken, New Jersey, United States.

37. Risch, M. (2017) Perovskite Electrocatalysts for the Oxygen Reduction Reaction in Alkaline Media. *Catalysts*, **7** (5), 154.

38. Bera, A.K., and Yusuf, S.M. (2021) Functional Perovskites: Structure-Properties Correlations, in *Perovskites and other Framework Structure Crystalline Materials*, vol. 5, OAJ Materials and Devices, pp. 39.

39. Zhu, J., Li, H., Zhong, L., Xiao, P., Xu, X., Yang, X., Zhao, Z., and Li, J. (2014) Perovskite Oxides: Preparation, Characterizations, and Applications in Heterogeneous Catalysis. *ACS Catal*, **4** (9), 2917–2940.

40. Yuan, L., Huang, K., Wang, S., Hou, C., Wu, X., Zou, B., and Feng, S. (2016) Crystal Shape Tailoring in Perovskite Structure Rare-Earth Ferrites $REFeO_3$ (RE = La, Pr, Sm, Dy, Er, and Y) and Shape-Dependent Magnetic Properties of YFeO3. *Cryst Growth Des*, **16** (11), 6522–6530.

41. Zhou, Z., Guo, L., Yang, H., Liu, Q., and Ye, F. (2014) Hydrothermal synthesis and magnetic properties of multiferroic rare-earth orthoferrites. *J Alloys Compd*, **583**, 21–31.

42. Yuan, X.P., Tang, Y.K., Sun, Y., and Xu, M.X. (2012) Structure and magnetic properties of $Y_{1-x}Lu_xFeO_3$ ($0 \leq x \leq 1$) ceramics. *J Appl Phys*, **111** (5).

43. Vopson, M.M. (2015) Fundamentals of Multiferroic Materials and Their Possible Applications. *Crit Rev in Solid State and Mat Science*, **40** (4), 223–250.

44. Hosokawa, S. (2019) Hexagonal Rare Earth-Iron Mixed Oxides ($REFeO_3$): Crystal Structure, Synthesis, and Catalytic Properties. *Front Chem*, **7** (8).

45. Lisi, L., Bagnasco, G., Ciambelli, P., De Rossi, S., Porta, P., Russo, G., and Turco, M. (1999) Perovskite-type oxides: II. Redox properties of $LaMn_{1-x}Cu_xO_3$ and $LaCo_{1-x}Cu_xO_3$ and methane catalytic combustion. *J Solid State Chem*, **146** (1), 176–183.

46. Tokunaga, Y., Furukawa, N., Sakai, H., Taguchi, Y., Arima, T.H., and Tokura, Y. (2009) Composite domain walls in a multiferroic perovskite ferrite. *Nat Mater*, **8** (7), 558–562.

47. Chen, L., Jiang, T., Zheng, G., Yao, G., Wang, L., Yang, Y., Zheng, H., Jiang, Y., Lu, Y., and Wei, S. (2021) Narrow-Bandgap Semiconductors of Perovskite Rare-Earth Orthoferrites (REFeO3). *Current Chinese Science*, **1** (4), 438–452.

48. Tikhanova, S., Seroglazova, A., Chebanenko, M., Nevedomskiy, V., and Popkov, V. (2022) Effect of TiO_2 Additives on the Stabilization of h-$YbFeO_3$ and Promotion of Photo-Fenton Activity of o-$YbFeO_3$/h-$YbFeO_3$/r-TiO_2 Nanocomposites. *Materials*, **15** (22), 8273.

49. Zhang, J., Huang, K., Yuan, L., and Feng, S. (2018) Mineralizer effect on facet-controllable hydrothermal crystallization of perovskite structure $YbFeO_3$ crystals. *CrystEngComm*, **20** (4), 470–476.

50. Wang, Z.Q., Lan, Y.S., Zeng, Z.Y., Chen, X.R., and Chen, Q.F. (2019) Magnetic structures and optical properties of rare-earth orthoferrites $RFeO_3$ (R = Ho, Er, Tm and Lu). *Solid State Commun*, **288**, 10–17.

51. Tikhanova, S.M., Lebedev, L.A., Kirillova, S.A., Tomkovich, M. V., and Popkov, V.I. (2021) Synthesis, structure, and visible-light-driven activity of *o*-$YbFeO_3$/*h*-$YbFeO_3$/CeO_2 photocatalysts. *Chimica Techno Acta*, **8** (4).

52. Demazeau, G. (1999) Materials Solvothermal processes: a route to the stabilization of new materials. *J Mater Chem*, **9**, 15–18.

53. Byrappa, K., and Yoshimura, M. (2001) *Handbook of hydrothermal technology : a technology for crystal growth and materials processing*, Noyes Publications, Park Ridge, New Jersey, U.S.A.

54. Li, J., Chen, Z., Wang, R.-J., and Proserpio, D.M. (1999) Low temperature route towards new materials: solvothermal synthesis of metal chalcogenides in ethylenediamine. *Coord Chem Rev*, **190**, 707–735.

55. Diodati, S., Dolcet, P., Casarin, M., and Gross, S. (2015) Pursuing the Crystallization of Mono- and Polymetallic Nanosized Crystalline Inorganic Compounds by Low-Temperature Wet-Chemistry and Colloidal Routes. *Chem Rev*, **115** (20), 11449–11502.

56. Cansell, F., Chevalier, B., Demourgues, A., Etourneau, J., Even, C., Garrabos, Y., Pessey, V., Petit, S., Tressaud, A., and Weill, F. (1999) Supercritical fluid processing: a new route for materials synthesis. *J Mater Chem*, **9** (1), 67–75.

57. Somiya, S., and Roy, R. (2000) Hydrothermal synthesis of fine oxide powders. *Bulletin of Materials Science*, **23**, 453–460.

58. Rajamathi, M., and Seshadri, R. (2002) Oxide and chalcogenide nanoparticles from hydrothermal/solvothermal reactions. *Curr Opin Solid State Mater Sci*, **6** (4), 337–345.

59. Livage, J. (2010) Hydrothermal synthesis of nanostructured vanadium oxides. *Materials*, **3** (8), 4175–4195.

60. Modeshia, D.R., and Walton, R.I. (2010) Solvothermal synthesis of perovskites and pyrochlores: Crystallisation of functional oxides under mild conditions. *Chem Soc Rev*, **39** (11), 4303–4325.

61. Polarz, S. (2011) Shape Matters: Anisotropy of the Morphology of Inorganic Colloidal Particles – Synthesis and Function. *Adv Funct Mater*, **21** (17), 3214–3230.

62. Teora, S.P., Panavaité, E., Sun, M., Kiffen, B., and Wilson, D.A. (2023) Anisotropic, Hydrogel Microparticles as pH-Responsive Drug Carriers for Oral Administration of 5-FU. *Pharmaceutics*, **15** (5), 1380.

63. Sun, X.-T., Liu, M., and Xu, Z.-R. (2014) Microfluidic fabrication of multifunctional particles and their analytical applications. *Talanta*, **121**, 163–177.

64. Wang, Z.L. (2000) Transmission Electron Microscopy of Shape-Controlled Nanocrystals and Their Assemblies. *J Phys Chem B*, **104** (6), 1153–1175.

65. Bhol, P., Bhavya, M.B., Swain, S., Saxena, M., and Samal, A.K. (2020) Modern Chemical Routes for the Controlled Synthesis of Anisotropic Bimetallic Nanostructures and Their Application in Catalysis. *Front Chem*, **8**.

66. Arandiyan, H., Wang, Y., Parlett, C.M.A., and Lee, A.F. (2021) Hierarchical and Anisotropic Nanostructured Catalysts, in *Heterogeneous Catalysts*, vol. 1–2, Wiley, pp. 161–181.

67. Pearce, A.K., Wilks, T.R., Arno, M.C., and O'Reilly, R.K. (2021) Synthesis and applications of anisotropic nanoparticles with precisely defined dimensions. *Nat Rev Chem*, **5** (1), 21–45.

68. Wang, S., Wang, X., Yuan, L., Ma, G., Zhang, J., Zhang, Y., Cui, X., Wu, X., and Lu, D. (2020) Shape Controllable Synthesis of Bi-Based Perovskite Superconductor Microcrystals via a Mild Hydrothermal Method. *Cryst Growth Des*, **20** (4), 2123–2128.

69. Yang, X., Xu, G., Ren, Z., Wei, X., Chao, C., Gong, S., Shen, G., and Han, G. (2014) The hydrothermal synthesis and formation mechanism of single-crystalline perovskite $BiFeO_3$ microplates with dominant (012) facets. *CrystEngComm*, **16** (20), 4176–4182.

70. Shang, Y., and Guo, L. (2015) Facet-Controlled Synthetic Strategy of Cu_2O-Based Crystals for Catalysis and Sensing. *Adv Sci*, **2** (10).

71. Liu, G., Yang, H.G., Pan, J., Yang, Y.Q., Lu, G.Q.M., and Cheng, H.M. (2014) Titanium dioxide crystals with tailored facets. *Chem Rev*, **114** (19), 9559–9612.

72. Hojamberdiev, M., Xu, Y., Wang, F., Wang, J., Liu, W., and Wang, M. (2009) Morphology-Controlled Hydrothermal Synthesis of Bismuth Ferrite Using Various Alkaline Mineralizers. *Ceramics-Silikaty*, **53** (2), 113–117.

73. Shannon, R.D. (1976) Revised Effective Ionic Radii and Systematic Studies of Interatomie Distances in Halides and Chaleogenides. *Acta Cryst*, **32**.

74. Neagu, D., Tsekouras, G., Miller, D.N., Ménard, H., and Irvine, J.T.S. (2013) In situ growth of nanoparticles through control of non-stoichiometry. *Nat Chem*, **5** (11), 916–923.

75. Neagu, D., Oh, T.-S., Miller, D.N., Ménard, H., Bukhari, S.M., Gamble, S.R., Gorte, R.J., Vohs, J.M., and Irvine, J.T.S. (2015) Nano-socketed nickel particles with enhanced coking resistance grown in situ by redox exsolution. *Nat Commun*, **6** (1), 8120.

76. Katz, M.B., Graham, G.W., Duan, Y., Liu, H., Adamo, C., Schlom, D.G., and Pan, X. (2011) Self-Regeneration of Pd–$LaFeO_3$ Catalysts: New Insight from Atomic-Resolution Electron Microscopy. *J Am Chem Soc*, **133** (45), 18090–18093.

77. Ma, J., Geng, Z., Jiang, Y., Hou, X., Ge, X., Wang, Z., Huang, K., Zhang, W., and Feng, S. (2021) Exsolution manipulated local surface cobalt/iron alloying and dealloying conversion in $La_{0.95}Fe_{0.8}Co_{0.2}O_3$ perovskite for oxygen evolution reaction. *J Alloys Compd*, **854**, 157154.

78. Cong, Y., Geng, Z., Zhu, Q., Hou, H., Wu, X., Wang, X., Huang, K., and Feng, S. (2021) Cation-Exchange-Induced Metal and Alloy Dual-Exsolution in Perovskite Ferrite Oxides Boosting the Performance of Li-O_2 Battery. *Ang Chem Intern Ed*, **60** (43), 23380–23387.

79. Sajid, A., Pervaiz, E., Ali, H., Noor, T., and Baig, M.M. (2022) A perspective on development of fuel cell materials: Electrodes and electrolyte. *Int J Energy Res*, **46** (6), 6953–6988.

80. Tang, C., Kousi, K., Neagu, D., and Metcalfe, I.S. (2021) Trends and Prospects of Bimetallic Exsolution. *Chem Eu J*, **27** (22), 6666–6675.

81. Sun, Z., Hao, C., Toan, S., Zhang, R., Li, H., Wu, Y., Liu, H., and Sun, Z. (2023) Recent advances in exsolved perovskite oxide construction: exsolution theory, modulation, challenges, and prospects. *J Mater Chem A Mater*, **6** (207890), 121.

82. Kim, Y.H., Kang, Y., Jo, S., Jeong, H., Neagu, D., and Myung, J. ha (2022) Shape-shifting nanoparticles on a perovskite oxide for highly stable and active heterogeneous catalysis. *Chemical Engineering Journal*, **441**.

83. Gao, Y., Lu, Z., You, T.L., Wang, J., Xie, L., He, J., and Ciucci, F. (2018) Energetics of Nanoparticle Exsolution from Perovskite Oxides. *J Phy Chem Lett*, **9** (13), 3772–3778.

84. Bai, L., Polo-Garzon, F., Bao, Z., Luo, S., Moskowitz, B.M., Tian, H., and Wu, Z. (2019) Impact of Surface Composition of $SrTiO_3$ Catalysts for Oxidative Coupling of Methane. *ChemCatChem*, **11** (8), 2107–2117.

85. Tilley, R.J. (2006) *Crystals and Crystal Structures*, John Wiley & Sons, Southern Gate, Chichester, West Sussex, England.

86. Bragg, W.H., and Bragg, W.L. (1913) The reflection of X-rays by crystals. *Proceedings of the Royal Society of London. Series A, Containing Papers of a Mathematical and Physical Character*, **88** (605), 428–438.

87. Bunaciu, A.A., Udriştioiu, E. gabriela, and Aboul-Enein, H.Y. (2015) X-Ray Diffraction: Instrumentation and Applications. *Crit Rev Anal Chem*, **45** (4), 289–299.

88. Inoue, M., and Hirasawa, I. (2013) The relationship between crystal morphology and XRD peak intensity on $CaSO_4{\cdot}2H_2O$. *J Cryst Growth*, **380**, 169–175.

89. Holder, C.F., and Schaak, R.E. (2019) Tutorial on Powder X-ray Diffraction for Characterizing Nanoscale Materials. *ACS Nano*, **13** (7), 7359–7365.

90. Jian, Z., and HElING, W. (2003) The Physical Meanings of 5 Basic Parameters for an X-Ray Diffraction Peak and Their Application. *Chin J Geochem*, **22** (1).

91. Akhtar, K., Khan, S.A., Khan, S.B., and Asiri, A.M. (2018) Scanning electron microscopy: Principle and applications in nanomaterials characterization, in *Handbook of Materials Characterization*, Springer Cham, Berlin, Germany, pp. 113–145.

92. Zhou, W., Apkarian, R.P., Lin Wang, Z., and Joy, D. (2007) Fundamentals of Scanning Electron Microscopy (SEM), in *Scanning Microscopy for Nanotechnology: Techniques and Applications*, Springer, New York, USA, pp. 1–40.

93. Paré, J.R.J., and Yaylayan, V. (1997) Mass Spectrometry: and Applications Principles, in *Techniques and instrumentation in analytical chemistry*, vol. 18, Elsever, Amsterdam, Netherlands, pp. 239–265.

94. Reiche CH-, M., Maciejewski CH-, M., Baiker CH-, A., Reiche, M., Maciejewski, M., Berndt, H., Kürschner, U., Brückner, A., Baerns D-, M., del Arco, M., Martín, C., Rives E-, V., Nogier F-, Jp., Praliaud, H., Pommier, B., and Varloud F-, J. (2000) Characterization by temperature programmed reduction. *Catal Today*, **56**.

95. Wang, J., Kalaev, D., Yang, J., Waluyo, I., Hunt, A., Sadowski, J.T., Tuller, H.L., and Yildiz, B. (2023) Fast Surface Oxygen Release Kinetics Accelerate Nanoparticle Exsolution in Perovskite Oxides. *J Am Chem Soc*, **145** (3), 1714–1727.

96. Rudolph, B., Tsiotsias, A.I., Ehrhardt, B., Dolcet, P., Gross, S., Haas, S., Charisou, N.D., Goula, M.A., and Mascotto, S. (2023) Nanoparticle Exsolution from Nanoporous Perovskites for Highly Active and Stable Catalysts. *Adv Sci*, **10** (6).

97. Henderson, G.S., de Groot, F.M.F., and Moulton, B.J.A. (2014) X-ray absorption near-edge structure (XANES) spectroscopy, in *Spectroscopic Methods in Mineralogy and Materials Sciences*, De Gruyter, Berlin, Boston, USA, pp. 75–138.

98. Newville, M. (2004) Fundamentals of XAFS. *Consortium for Advanced Radiation Sources, University of Chicago*, **78**.

99. Bianconi, A. (1980) SURFACE X-RAY ABSORPTION SPECTROSCOPY: SURFACE EXAFS AND SURFACE XANES. *Appl of Surf Sci*, **6**, 392–418.

100. Rehr, J.J., and Albers, R.C. (2000) Theoretical approaches to x-ray absorption fine structure. *Rev Mod Phys*, **72** (3), 621–654.

101. Zhang, N., Wang, W., Zhou, T., Tian, Y., and Chu, W. (2020) Exploring Structure-function Relationship of Two-dimensional Electrocatalysts with Synchrotron Radiation X-ray Absorption Spectrum. *Curr Chin Sci*, **1** (1), 22–42.

102. Iglesias-Juez, A., Chiarello, G.L., Patience, G.S., and Guerrero-Pérez, M.O. (2022) Experimental methods in chemical engineering: X-ray absorption spectroscopy— XAS, XANES, EXAFS. *Can J Chem Eng*, **100** (1), 3–22.

103. Marezio, M., Remeika, J.P., and Dernier, P.D. (1970) The crystal chemistry of the rare earth orthoferrites. *Acta Crystallogr B*, **26** (12), 2008–2022.

104. Pauling L, Hendricks, S.B. (1925) The Crystal Structures of Hematite and Corundum. *J Am Chem Soc*, **47** (1924), 781–790.

105. Li, Z., Abdulvakhidov, K., Abdulvakhidov, B., Soldatov, A., Nazarenko, A., Plyaka, P., Manukyan, A., Angadi, V.J., Shapovalova, S., Sirota, M., Vitchenko, M., Mardasova, I., Ubushaeva, E., Kallaev, S., and Omarov, Z. (2022) Influence of mechanical activation on crystal structure and physical properties of YbFeO3. *Appl Phys A Mater Sci Process*, **128** (12), 1–12.

106. Zhang, L., Gonçalves, A.A.S., and Jaroniec, M. (2020) Identification of preferentially exposed crystal facets by X-ray diffraction. *RSC Adv*, **10** (10), 5585–5589.

107. Gerbreders, V., Krasovska, M., Sledevskis, E., Gerbreders, A., Mihailova, I., Tamanis, E., and Ogurcovs, A. (2020) Hydrothermal synthesis of ZnO nanostructures with controllable morphology change. *CrystEngComm*, **22** (8), 1346–1358.

108. Pinceloup, P., Courtois, C., Vicens, J., Leriche, A., and Thierry, B. (1999) Evidence of a Dissolution-Precipitation Mechanism in Hydrothermal Synthesis of Barium Titanate Powders. *J Eur Ceram Soc*, **19** (6–7), 973–977.

109. Maxim, F., Ferreira, P., Vilarinho, P.M., and Reaney, I. (2008) Hydrothermal Synthesis and Crystal Growth Studies of $BaTiO_3$ Using Ti Nanotube Precursors. *Cryst Growth Des*, **8** (9), 3309–3315.

110. Kim, J.H., Kim, J.K., Liu, J., Curcio, A., Jang, J.S., Kim, I.D., Ciucci, F., and Jung, W.C. (2021) Nanoparticle Ex-solution for Supported Catalysts: Materials Design, Mechanism and Future Perspectives. *ACS Nano*, **15** (1), 81–110.

111. Garces, L.J., Hincapie, B., Zerger, R., and Suib, S.L. (2015) The Effect of Temperature and Support on the Reduction of Cobalt Oxide: An in Situ X-ray Diffraction Study. *The Journal of Physical Chemistry C*, **119** (10), 5484–5490.

112. Polat, O., Coskun, M., Coskun, F.M., Zlamal, J., Kurt, B.Z., Durmus, Z., Caglar, M., and Turut, A. (2019) Co doped $YbFeO_3$: exploring the electrical properties via tuning the doping level. *Ionics*, **25** (8), 4013–4029.

113. Shanbhag, P.N., Biswas, R.K., Pati, S.K., Sundaresan, A., and Rao, C.N.R. (2020) Elusive Co_2O_3: A Combined Experimental and Theoretical Study. *ACS Omega*, **5** (45), 29009–29016.

114. Wang, J., Syed, K., Ning, S., Waluyo, I., Hunt, A., Crumlin, E.J., Opitz, A.K., Ross, C.A., Bowman, W.J., and Yildiz, B. (2022) Exsolution Synthesis of Nanocomposite Perovskites with Tunable Electrical and Magnetic Properties. *Adv Funct Mater*, **32** (9).

115. Wang, Y., Zhang, C., Liu, F., and He, H. (2013) Well-dispersed palladium supported on ordered mesoporous Co_3O_4 for catalytic oxidation of o-xylene. *Appl Catal B*, **142–143**, 72–79.

116. Khodaei, M., Seyyed Ebrahimi, S.A., Park, Y.J., Choi, S.H., Kim, C., Son, J., and Baik, S. (2013) (111)-Oriented $Co_{0.8}Fe_{2.2}O_{4+\delta}$ thin film grown by pulsed laser deposition: Structural and magnetic properties. *J Mater Sci*, **48** (20), 6960–6969.

117. Diodati, S., Walton, R.I., Mascotto, S., and Gross, S. (2020) Low-temperature wet chemistry synthetic approaches towards ferrites. *Inorg Chem Front*, **7** (18), 3282–3314.

118. Feng, G., Cheng, P., Yan, W., Borona, M., Li, X., Su, J.H., Wang, J., Li, Y., Corma, A., Xu, R., and Yu, J. (2016) Accelerated crystallization of zeolites via hydroxyl free radicals. *Science*, **351** (6278), 1188–1191.

119. Holden, A., and Singer, P. (1971) *Crystals and Crystal Growing* , Anchor Books Doubleday & Company Inc., Garden City, New York.

120. Saravanan, T., Anandan, P., Shanmugam, M., Azhagurajan, M., Mohamed Ismail, M., Arivanandhan, M., Hayakawa, Y., and Jayavel, R. (2020) Facile synthesis of Yb_2O_3–graphene nanocomposites for enhanced energy and environmental applications. *Polymer Bulletin*, **77** (8), 3891–3906.

121. Morris, M.C., McMurdie, H.F., Evans, E.H., Paretzkin, B., Parker, H.S., Wong-Ng, W., and Gladhill, D.M. (1985) *Standard X-ray Powder Patterns*, Department of Commerce, National Bureau of Standards, Institute for Materials Research.

122. Poffe, E., Kaper, H., Ehrhardt, B., Gigli, L., Aubert, D., Nodari, L., Gross, S., and Mascotto, S. (2021) Understanding Oxygen Release from Nanoporous Perovskite Oxides and Its

Effect on the Catalytic Oxidation of CH_4 and CO. *ACS Appl Mater Interfaces*, **13** (21), 25483–25492.

123. Zhao, K., He, F., Huang, Z., Wei, G., Zheng, A., Li, H., and Zhao, Z. (2016) Perovskite-type oxides $LaFe_{1-x}Co_xO_3$ for chemical looping steam methane reforming to syngas and hydrogen co-production. *Appl Energy*, **168**, 193–203.

124. Roseno, K.T.C., Brackmann, R., da Silva, M.A., and Schmal, M. (2016) Investigation of $LaCoO_3$, $LaFeO_3$ and $LaCo_{0.5}Fe_{0.5}O_3$ perovskites as catalyst precursors for syngas production by partial oxidation of methane. *Int J Hydrogen Energy*, **41** (40), 18178–18192.

125. Guda, A.A., Guda, S.A., Martini, A., Kravtsova, A.N., Algasov, A., Bugaev, A., Kubrin, S.P., Guda, L. V., Šot, P., van Bokhoven, J.A., Copéret, C., and Soldatov, A. V. (2021) Understanding X-ray absorption spectra by means of descriptors and machine learning algorithms. *NPJ Comput Mater*, **7** (1), 203.

126. Arman, M.M., Imam, N.G., Loredo Portales, R., and El-Dek, S.I. (2020) Synchrotron radiation X-ray absorption fine structure and magnetization improvement of A-site Ce3+ doped $LaFeO_3$. *J Magn Magn Mater*, **513**, 167097.

127. Kothari, D., Upadhya, S., Meneghini, C., Reddy, V.R., Aquilanti, G., and Gupta, A. (2012) Structural and magnetic study of la doped multiferroic $BiFeO_3$. *AIP Conf Proc*, **1447** (1), 1319–1320.

128. Kim, J., Ferree, M., Gunduz, S., Millet, J.M.M., Aouine, M., Co, A.C., and Ozkan, U.S. (2022) Exsolution of nanoparticles on A-site-deficient lanthanum ferrite perovskites: Its effect on co-electrolysis of CO_2 and H_2O. *J Mater Chem A Mater*, **10** (5), 2483–2495.

129. Kwon, O., Sengodan, S., Kim, K., Kim, G., Jeong, H.Y., Shin, J., Ju, Y.-W., Han, J.W., and Kim, G. (2017) Exsolution trends and co-segregation aspects of self-grown catalyst nanoparticles in perovskites. *Nat Commun*, **8**, 15967.

130. Wang, C., Lv, R., Huang, Z., Kang, F., and Gu, J. (2011) Synthesis and microwave absorbing properties of FeCo alloy particles/graphite nanoflake composites. *J Alloys Compd*, **509** (2), 494–498.

131. Brackmann, R., Perez, C.A., and Schmal, M. (2014) $LaCoO_3$ perovskite on ceramic monoliths - Pre and post reaction analyzes of the partial oxidation of methane. *Int J Hydrogen Energy*, **39** (26), 13991–14007.

132. Thalinger, R., Gocyla, M., Heggen, M., Klötzer, B., and Penner, S. (2015) Exsolution of Fe and SrO Nanorods and Nanoparticles from Lanthanum Strontium Ferrite $La_{0.6}Sr_{0.4}FeO_{3-\delta}$ Materials by Hydrogen Reduction. *The Journal of Physical Chemistry C*, **119** (38), 22050–22056.

133. Wang, J., Kumar, A., Wardini, J.L., Zhang, Z., Zhou, H., Crumlin, E.J., Sadowski, J.T., Woller, K.B., Bowman, W.J., Lebeau, J.M., and Yildiz, B. (2022) Exsolution-Driven Surface Transformation in the Host Oxide. *Nano Lett*, **22** (13), 5401–5408.

134. Lv, H., Lin, L., Zhang, X., Song, Y., Matsumoto, H., Zeng, C., Ta, N., Liu, W., Gao, D., Wang, G., and Bao, X. (2020) In Situ Investigation of Reversible Exsolution/Dissolution of CoFe Alloy Nanoparticles in a Co-Doped $Sr_2Fe_{1.5}Mo_{0.5}O_{6-\delta}$ Cathode for CO_2 Electrolysis. *Adv Mater*, **32** (6), 1906193.

10 Acknowledgements

Desidero ringraziare i miei relatori, la Professoressa Silvia Gross e il Professor Simone Mascotto per la grande disponibilità, cortesia, competenza ed entusiasmo che hanno sempre trasmesso nei confronti di questo lavoro di tesi. Ringrazio la professoressa Gross per avermi incoraggiata a fare domanda per la borsa Erasmus e assistito durante questa esperienza, che definirei essere stata la ciliegina su quella torta che è l'Università. Ringrazio dunque il professor Simone Mascotto per avermi dato la possibilità di effettuare questa esperienza all'estero da cui tanto ho imparato, per avermi assegnato questo entusiasmante progetto di tesi e per avermi permesso di partecipare sia ad una conferenza che ad un beamtime che mi hanno permesso di vedere ancora più da vicino l'affascinante mondo della ricerca scientifica. Durate il mio periodo di tesi, presso l'Università di Amburgo, ho avuto il piacere di lavorare nei laboratori del Professor Michael Fröba, che ringrazio molto per l'accoglienza e l'amichevolezza dimostratami da tutto il suo gruppo di ricerca.

Un particolare e caloroso ringraziamento va agli studenti dottorandi del gruppo di ricerca del Prof. Mascotto: Emna, Benny e Filippo, i quali non sono stati solo colleghi ma anche ottimi insegnanti ed amici. Emna, un grazie particolare va a te, alla tua pazienza ed alla tua calma con cui mi hai affiancata in tutti questi mesi.

Per me Università significa anche amicizia e condivisione e questo lo devo a tutte le persone speciali che ho incontrato durante questi anni. Grazie soprattutto a Chiara, Dinny, Gloria, Lorenza, Sara, Gio, Miki, Manuel e Piero per tutte le avventure patavine (e non solo), le risate, le cene colorate e le sessioni di studio in compagnia. Ad Arianna, Francesca e Margherita, le coinquiline che ogni studente fuori sede dovrebbe avere, con cui ho creato una seconda famiglia in casa di Vicolo Ognissanti.

Grazie di cuore alle amiche di una vita Cecilia e Matilda, quelle persone su cui sai sempre di poter contare e che senti sempre vicine anche nella lontananza. Un grazie speciale va a Jacopo, che con quella sua gentilezza e vivacità, è sempre stato dalla mia parte, che è sempre riuscito a capirmi e sostenermi.

Infinite grazie ai miei familiari. A mia sorella Aurora, la mia confidente e punto di forza nei momenti più duri. Ai miei genitori senza i quali tutto ciò non sarebbe stato possibile, che mi hanno sempre supportata in ogni mia decisione, spronandomi alla curiosità e alla determinazione. A voi dedico questo successo e ve ne sono infinitamente grata.

I would like to thank my supervisors, Professor Silvia Gross and Professor Simone Mascotto for their great helpfulness, courtesy, competence and enthusiasm that they have always conveyed towards this thesis work. I thank Professor Gross for encouraging me to apply for the Erasmus+ and assisting me during this experience, which I would define as having been the cherry on the cake that is University. So I thank Professor Simone Mascotto for giving me the opportunity to carry out this experience abroad from which I learned so much, for assigning me this exciting thesis project, and for allowing me to attend both a conference and a beamtime that allowed me to see the fascinating world of scientific research even more closely. During my thesis period, at the University of Hamburg, I had the pleasure of working in the laboratories of Professor Michael Fröba, whom I thank very much for the welcome and friendliness shown to me by his entire research group.

A special and warm thanks goes to the PhD students in Prof. Mascotto's research group: Emna, Benny and Filippo who were not only colleagues but also excellent teachers and friends. Emna, a special thanks goes to you, to your patience and calmness with which you have stood by me all these months.

For me University also means friendship and sharing, and this I owe to all the special people I have met during these years. Thanks especially to Chiara, Dinny, Gloria, Lorenza, Sara, Gio, Miki, Manuel, and Piero for all the Patavine (and other) adventures, laughs, colorful dinners, and study sessions together. To Arianna, Francesca and Margherita, the roommates every off-campus student should have, with whom I have created a second family in Vicolo Ognissanti’s house.

Many thanks to lifelong friends Cecilia and Matilda, those people you always know you can count on and who you always feel close to you even in the distance. A special thank you goes to Jacopo, who with that kindness and liveliness, was always on my side, who always managed to understand and support me.

Endless thanks to my family members. To my sister Aurora, my confidante and point of strength in the hardest moments. To my parents without whom none of this would have been possible, who always supported me in every decision I made, spurring me on to curiosity and determination. To you I dedicate this success and I am infinitely grateful.